Università Cattolica del Sacro Cuore
Sede di Brescia

Facoltà di Scienze Matematiche, Fisiche e Naturali
Corso di Laurea in Fisica

Tesi di Laurea Magistrale

Time resolved Microscopy on nanostructured materials

Relatore:
Dott. Francesco Banfi
Correlatore:
Dott. Gabriele Ferrini

Laureando: **Sterzi Andrea**
mat. 3910005

Anno Accademico 2011/2012

Contents

Chapter 1

Introduction

1.1 Overview

Over the last decades the scientific and technological interest in thermomechanics at the nanoscale has been significantly growing. Among the most relevant topics are metal nanoparticles (NPS). Metal NPS in fact possess novel properties suitable for a variety of applications ranging from photothermal cancer therapy to in-situ drug delivery. The basic idea underlying the applications is selective thermal energy delivery in form of heat transfer from the nanoparticles to the environment. The understanding of the thermomechanical dynamics is crucial in view of applications [3].

Conventional calorimetry is strongly limited when the size of the system under investigation reaches the sub-micron scale. A fast non contact probe is an optimal choice, the speed requirement being dictated by the fact that the time for heat exchange between the sample and the thermal reservoir is proportional to the sample mass. Over the last years experiments and all-optical schemes have been reported, this paved the way for all-optical time-resolved nanocalorimetry.

Pump & probe measurement, when performed on confined nano-objects, presents a lack. Studies of very long dynamics (ten of nanosecond) have not been conducted. As a matter of fact traditional pump & probe technique cannot investigate a scale of nanoseconds. The mechanical sampling method employs a mechanical delay and this is a limit that we want to overcome in the present work by using an asincronous optical system [16].

The basics of the sampling method will be reported and discussed. The detection of the nano-object is fundamental in oder to perform measurements. During the present thesis we have developed an instrument, the Nanoscope, to fulfil this purpose. Moreover different techniques for the nanoparticle detection employing the nanoscope have been tested and described.

1.2 Outline

The first chapter introduces the thermodynamics of a single metal nanodisk excited by an ultrafast laser pulse. A simple analytical model for the thermal dynamics is outlined. The second chapter explains the experimental set-up, the nanoscope and the operative procedures are described in detail. The third chapter covers both the theory and implementation of spatial modulation nanoscopy. A deep study of the theory and the numerical models is reported. Furthermore we tested the spatial modulation on a single nanodisk and compared the experimental results to the numerical simulations.
The last chapter focuses on the pump & probe measurements on a single nanodisk of subwavelengths dimensions, covering the thermal dynamics from a ps to 10 ns. The experimental results have been fit and discussed. During the present thesis we tested and characterized different instruments in order to overcome the technical problems arisen. Appendices were added in order to collect information and annotations.

Chapter 2

Thermal impulsive dynamics of a template system

In this chapter we focus on the thermal dynamics triggered by a short laser pulse ($100fs$) on a template system which consist of an Al nanodisk 450 nm diameter and height 30 $nm\dot{I}$n the present thesis a similar system by means of the pump & probe technique is considered. The relations between the system sizes and thermal relaxations times will be discussed. Thermomechanics of a single metal nanodisk excited by an unltrafast laser pulse (defined *pump*), involves three processes spanning three different time scales [7].

1. In the first step the laser short pulse heats the electron gas of the metallic nanodisks (sub-picosecond time scale). The electromagnetic energy is absorbed by the electrons, as in the Drude model.
2. In the second step the hot electron gas thermalizes with the lattice (picosecond time scale). The thermalization of the disk is due to electrons-phonons scattering.
3. In the third step two phenomena are observed: a) an acoustic eigenmode is launched in the disks and transfers mechanical energy to the substrate. b) The disk thermalizes with the substrate. (nanosecond time scale)

Are presented in the block diagram these steps Fig. 2.1. Let's analyze the thermal

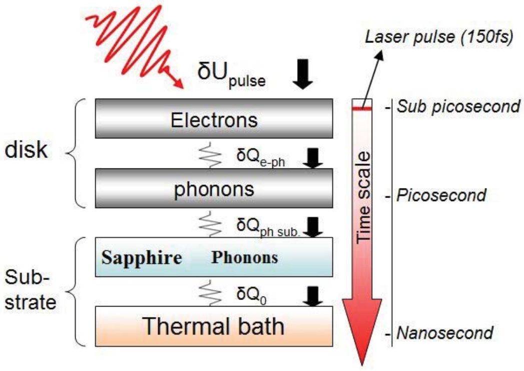

Figure 2.1: Schematic representation of the thermal dynamics following the laser pulse absorbtion. First two blocks represent the nanodisk and the heat transfer between electrons and phonons within the disk. The third and fourth blocks stand for the substrate and the thermal bath. At the right of the image, a time scale reports the processes' timing.

dynamics inherent step 3. Conservation of energy imposes:

$$-\nabla \cdot \mathbf{q} + g(\mathbf{r}, t) = \rho c_m \frac{\partial T}{\partial t} \tag{2.1}$$

where $g(\mathbf{r}, t)$ is the power density source term (W/m^3), $-\nabla \cdot \mathbf{q}$ the power density sink (W/m^3), $\mathbf{q}$ is the heat flux (W/m^2), and $\rho c_m \partial T/\partial t$ gives the instantaneous power density (ρ density of mass and c_m the specific heat for unity of mass). The Fourier equation can be considered as the constitutive equation for the thermal density current:

$$\mathbf{q} = -\kappa \nabla T.$$

So the conservation equation becomes:

$$\kappa \nabla^2 T + g(\mathbf{r}, t) = \rho c_m \frac{\partial T}{\partial t}. \tag{2.2}$$

The source term, according to our system, is given by the laser energy absorption. Aluminium shows an high thermal conductivity ($\kappa_{Al} = 237$ Wm^{-1}K^{-1} [8]), while the penetration depth of our *pump* laser at 1560 nm is Λ_{Al} is $\sim 7,45nm$ [9]). The aluminum disk's tickness is 30 nm hence we can assume that after the electron-phon thermalization takes place (few ps), the disk is isothermal at a temperature $T_0 \sim 300\ K$. The portion of laser energy absorbed by the Sapphire substrate is negligible. [1].

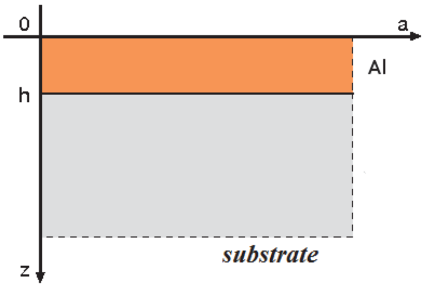

Figure 2.2: The geometry of a metal film deposited on a substrate chose as a model for the 1D thermal evolution problem [10].

Let's consider the simplest case for modeling the nanodisk, the film geometry is illustrated in Fig. 2.2.[2] This simplification reduces the thermal transfer to a 1D-problem which can be analitically resolved. At the film-substrate interface the heat transfer is conducted by the thermal boundary resistance ρ_{th} (m^{2}K/W) throughout the equation:

$$\kappa \frac{\partial T}{\partial z} = \frac{1}{\rho_{th}}[T(t) - T_{sub}].$$

We assume that no heat is lost to the air face: the following boundary condition applies at the film-air interface:

$$\frac{\partial T}{\partial z} = 0.$$

When the Biot's number, given by:

$$B = \frac{h}{\kappa \rho_{th}},$$

is $B \ll 1$, the solution of the thermal problem is simpler, in fact we have a single exponential decay of the temperature with a constant decay

$$\tau_{th} = (\rho c_m \rho_{th})h, \tag{2.3}$$

---

[1] The Sapphire Crystal which constitute our sample's sublayer it can be regarded as a thermal reservoir at a constant temperature T_{sub}

[2] Such simplification is all allowed because of the slender thickness of the film (30 nm), and the time for thermal diffusion in the planar direction exceed time for heat diffusion trough the film-substrate interface.

The term h stands for the *film*'s thickness. The thermal boundary resistance ρ_{th} of the interface Al/Sapphire is on the order of 10^{-8} m^2 K/W [12], considering $h = 30$ nm we get $B \sim 0.01$, thus satisfying $B \ll 1$.
The Aluminum mass densities at room temperature and specific heat capacity per unity mass are $\rho = 2700$ Kg m^{-3} and $c_m = 897$ JK^{-1} Kg^{-1} [9]. Applying the equation 2.3 we expect a decay time $\tau_{th} \sim 700$ ps. The thermal relaxation time is linear respect h as highlighted in the Graph in Fig. 2.3. This point will be discussed in depth further on.

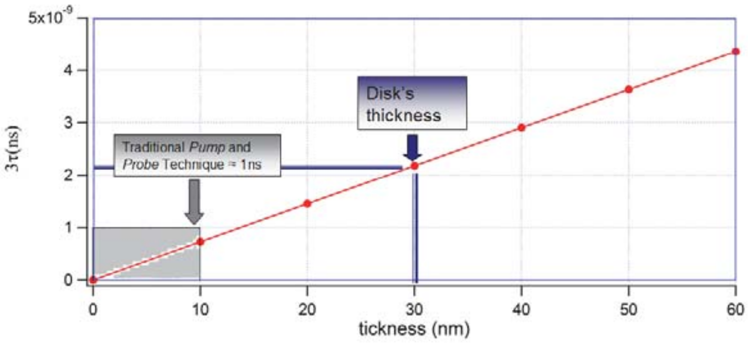

Figure 2.3: Linear dependence of the relaxation time with respect to the nanodisk' thickness h. We assume that the thermal relaxation occurs in 3τ. The grey rectangle indicates the limits of the traditional *pump* & *probe* technique.

The key message is that thermal relaxation times of *meso*- and *nano*-scale system occur on the time windows which scale with object's dimensions. Typical values are in the range of 100 ps to 10 ns for relevant sample's dimension in the 100 nm range. The percentage fluctuations in dimensions among different samples increase thus calling for measurements performed on single nano-objects.

Chapter 3

Time-resolved Microscopy

Our aim is to development a technique giving access to the thermomechanical dynamics of a single mettallic nanodisks. One needs :

- To focus the laser beam on a single nanodisk of subwavelength dimensions.
- Perform a time-resolved optical transmission measurement spanning a time window up to 10 ns.

Two techniques are exploited to satisfy the above mentioned needs. The first needs requires the spatial modulation and optical nanoscopy. The second requires the asynchronous optical sampling (Asops). The first section of the chapter centers upon the experimental setup because of its crucial role. First we present the Asops system and describe the optical set-up. We than illustrate the optical Nanoscope. The samples are illustrated in a separate section and explained in more depth . Laser beam characterization is presented in the last section. Operating procedures are summarized in the appendices.

3.1 Experimental setup

The first part of this section is dedicated to the *Asops* technique. We start analyzing the peculiarities of this *pump* & *probe* technique respect to the traditional one. Moreover the operating principles are illustrated. The nanoscope is illustrated in the second section.

We can see in Figure 3.1 an illustrations of both devices.

(a) Asops system (b) Nanoscope

Figure 3.1: The Laser source and the Nanoscope

3.1.1 Asops: Asynchronous Optical Sampling

The experimental technique used to realize time-resolved spectroscopy, nowadays used worldwide, is the *Pump* & *probe* technique. The constitutes one of the most diffused time resolved technique. The traditional approach uses a mechanical delay stage [1] and a laser beam[2]. The emitted beam is divided by a *beam splitter* into two different beams, one one being the pump and the latter the probe. The energy of pump beam is greater than in the probe beam.

In order to follow the relaxation dynamics of the sample between the two states (excited and normal) we must probe at successive instants of time. Pump and probe's pulse must be mutually delayed delayed by means of a mechanical delay stage or electronic delay. The commonly used method to obtain such time delay is the mechanical delay stage. The temporal delay is obtained guiding the *pump* pulse along a shorter path with respect the *probe* pulse. Typically a mirror is placed on the motor sledge, a motor stepper controls the position of the mirror and therefore the temporal delay between the two pulses. Every displacement δx corresponds to a delay $\delta t = \delta x/c$. This poses several

---

[1] Tipically a motor steps on a sledge, with a range of centimeters

[2] The laser ultrashort and impulsed

problems [15]:

- A long delay line implies difficulties in preserving the spatial coincidence between the *pump* and *probe* beams. Let's consider an experiment which employs a pump and a probe beam of diameter 1 and $0.5\mu m$ respectively. And let's assume we want to study temporal dynamic extending over 10 ns. In this case the *pump* and the *probe*'s beams should be maintained in coincidence with a spatial tolerance of 0.1 μm, while introducing a relative path difference ranging up to 3 m.
- Time for data acquisition grows a lot, because of the full displacement of the sledge. An extended measurement time poses problems related to instability.

These problems can be avoid using the Asynchronous Optical Sampling system *Asops*. Use of the Asops avoids mechanical delay stage. Henceforth, we indicate both laser source and sampling system, with *Asops*.

3.1.2 Operating principle

The system consists of two pulsed lasers at 780 nm and 1560 nm, with a temporal pulse length of about 150 fs. The method of asynchronous sampling is based on the fact that these laser sources have slightly different but stabilized pulse repetition rates. The pump and probe pulses have a repetition rate dictated by the frequencies ν_{pump} and ν_{probe} respectively. The values are $\nu_{pump} = 100\ MHz$ and $\nu_{probe} = 100MHz + \Delta\nu$. The frequency offset defined *detuning* $\Delta\nu$ is small with to the respect repetition rate. A schematic representation of the working principle is reported in fig. 3.2.

The detuning $\Delta\nu$ can be selected in the range $1Hz - 10KHz$. We now quantify the time window which is sampled in a measurement and the achievable temporal resolution. The delay time between two laser pulse is:

$$\Delta t = \left| \frac{1}{\nu_{pump}} - \frac{1}{\nu_{probe}} \right| = \frac{\Delta\nu}{\nu_{pump} \cdot \nu_{probe}}, \tag{3.1}$$

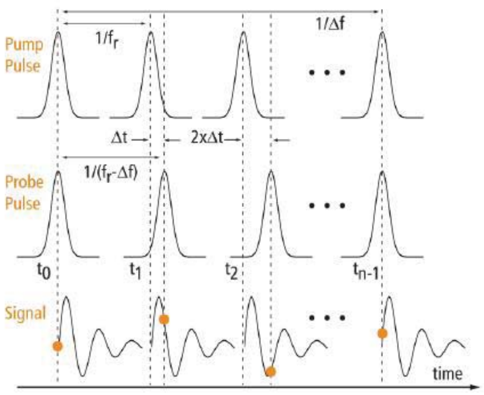

Figure 3.2: Asops's operating principle. Note that f_r stands for ν_{pomp} in text. Figure is taken from the manual [16]. The figure shows the relative temporal delay between the two pulses, which increase because of their frequency detuning

where $\Delta\nu$ is the *detuning*. Assuming that $\Delta\nu \ll \nu$, we can expand in series the last relation ($\nu_{probe} = \nu_{pump} + \Delta\nu$) getting:

$$\Delta t \approx \frac{\Delta\nu}{\nu_{pump}^2}. \tag{3.2}$$

The equation 3.2 gives the *temporal resolution* of a pump and probe measurement. Considering a typical detuning frequency of $1KHz$, we get a resolution of $10^{-13}s$.

The sampled time window is:

$$t_{window} = \frac{1}{\nu_{pump}} = \frac{1}{100\ MHz} = 10\ ns \tag{3.3}$$

We now want to evaluate the time in take to perform pump & probe measurement over the entire 10 ns delay time range (indicated as a pump & probe scan). The *probe* pulse accumulates a delay time Δt for every *pump* pulse, until they meet again after a fixed time interval t_0. Let's evaluate t_0, asking how many probe pulses m are needed to cover the time extent between two successive pulses[3]. Defining m as the number of pulses searched:

$$m(\Delta t) = \frac{1}{\nu_{pump}}$$

---

[3] The distance between the pump pulse is fixed, see Fig. 3.2

where the right-hand side is the distance in time between to successive pump pulse. Recalling relation 3.2:

$$m\left(\frac{\Delta\nu}{(\nu_{pump})^2}\right) = \frac{1}{\nu_{pump}} \tag{3.4}$$

so,

$$m = \frac{\nu_{pump}}{\Delta\nu_{pump}} \tag{3.5}$$

The value t_0 is related to m by:

$$t_0 = m\left(\frac{1}{\nu - \Delta\nu}\right) \tag{3.6}$$

Substituting m from equation 3.4 in 3.6 we obtain:

$$t_0 = \left(\frac{\nu_{pump}}{\Delta\nu_{pump}}\right)\frac{1}{\nu_{pump}}$$

$$t_0 \simeq \frac{1}{\Delta\nu_{pump}} \tag{3.7}$$

For istance setting a detuning frequency $\Delta\nu = 1KHz$, it takes 1 ms to perform a pump & probe measurement up to a time delay of 10 ns. To reduce the noise, several scans have to be performed, therefore increasing the time necessary to obtain a “clean“ experimental trace. Typically a “clean“ signal can be achieved integrating for minutes.

3.2 Optical setup

The optical set-up is reported in figure 3.3. The two laser cavities, the Nanoscope and detectors are depicted as black boxes. Mirrors and lens have different representations, the complete legend is reported below figure 3.3. The Photodetectors are labelled as “differential Photodetector“ and “1560“, the specific model that we have used are described in the appendix.

The pump beam (at 1560 nm) is guided in the nanoscope exploiting an high-reflectivity mirror (HR @ 45 @ 1560 nm)and two gold mirrors. The intensity of each beam is adjusted by an a half-wave plate coupled with a polarizer. A pin hole, with variable radius, is installed in front of the Nanoscope, in order to block a secondary beam at

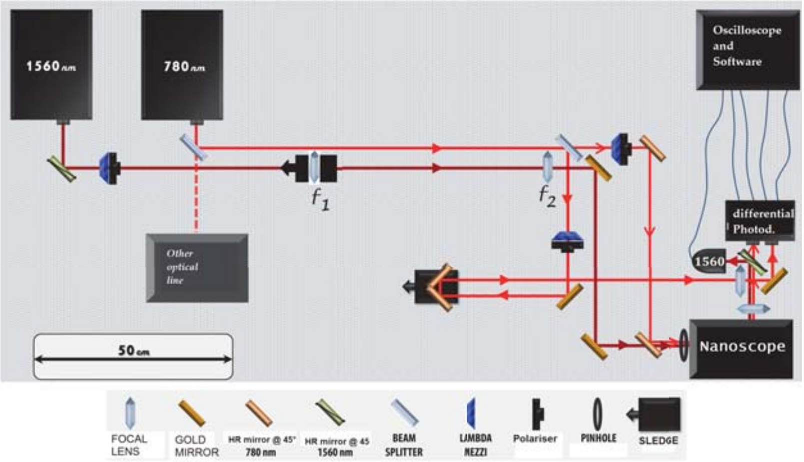

Figure 3.3: Scheme of the optical bench. Below for the optical lines' legend.

1560 *nm* originated by a double reflection effect.

Optical lines description

The *pump* beam leaves the laser cavity and passes through a *half wave plate* and *polarizer* intended for intensity control. f_1 and f_2 are two lenses forming an expanding telescope. The pump is reflected by a gold mirror, travels through the HR mirros for 780 and enters the Nanoscope. At the exit of the nanoscope a lens focuses the beam detected by a photodetector generally labelled as "1560". The beam is focused by a convex lens with a focal lenght of 10 *cm*, because of the small dimensions of the Si photodiode, .

The Probe beam (or 780 beam) is splitted twice by a 50/50 beam splitters. The first beam is used by another line, the second pertains to our line. A second 50/50 beam splitter is present. It deviates a portion of probe beam, that constitutes the reference line and is detected by a differential photodetector[4]. The mechanical sledge[5] supports two HR mirrors @ 45 @ 1560 *nm*. Through out the sledge's displacement, we can vary

---

[4] This beam 's path is controlled by the sledge illustrated in 3.3, this is due to the method of acquisition.

[5] Maximum range is 2.5 *cm* and 10 μm of resolution

the optical path of the reference probe beams. The ideal situation is when there's no difference between the probe beam and its reference. The fraction of the *probe* beam which is transmitted across the beam splitter after the passage in a half wave-plate, undergoes a double reflection by the two mirrors and enters the Nanoscope.

3.2.1 Nanoscope

The nanoscope is schematized In Fig. 3.4 togheter with the common path of both the pump & probe beams. This instrument is composed by four mirrors, two objectives and a CCD camera.

The two gold mirrorr reflect the beams on a HR mirror, the third mirrors of figure 3.4. This serves to focalize the beam into a 50*x Nikon* objective. In turn, the objective focalizes where the sample is to be located. An identical objective collects the divergent beam which travels through sample. An aluminum mirror leads the beam out of the nanoscope. The objective is a *50X Nikon CFI 60 LU Plan Epi ELWD.*

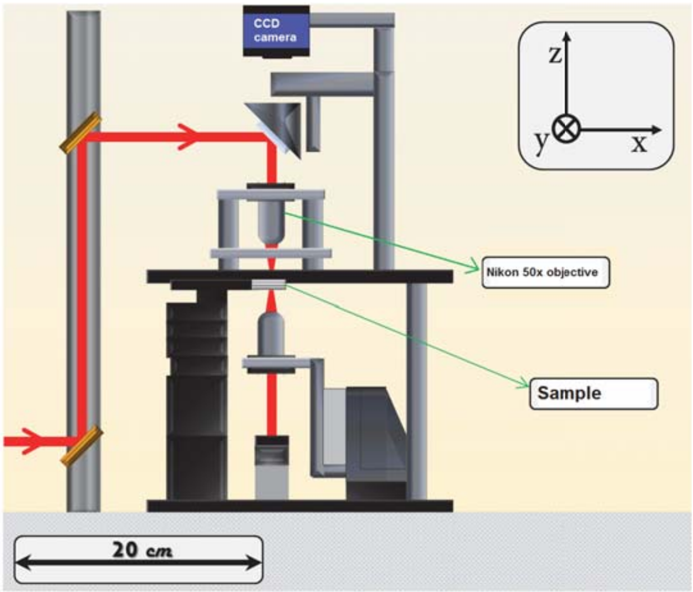

Figure 3.4: Nanoscope structure and beams' paths

The advantages of using the Nanoscope are:

- Focusing the probe beam (780 *nm*) to the diffraction limit, one can detect an object of dimension much lower than the wave lenght of the laser beam.
- Characterization and spatial control of the position of the laser beams.
- Optimization of the beams to perform the*pump* & *probe* measurements.
  We can locate the mutual position of two beams, in order to make them collinear and coincident on the sample, The phenomenon of chromatic aberration due to the first objective is exploited to ensure having probe beam of smaller dimension with respect to the pump. The pump beam ($\lambda = 780\ nm$), because of chromatic aberration, is focused at a superior height with respect to the probe beam.

The Nanoscope's components allow different regulations.

- Gold mirros can be rotated individually around the y and z axis, and can be shifted along the z direction.
- Upper HR mirror has similar regulations.
- The focusing objective rests on a tripods. Allowing height and and tilt control. The optical axis of the objective must be parallel to z, in order for be orthogonal to the sample.
- The sample holder is located between the two objectives. Fine and coarse adjustments are possible. The “coarse“ is dealt with two micrometer screws which, through a sledge, allow a displacement along x and y with a 10 μm precision. The “fine“ adjustment is achieved with a motorized actuator [6] controlled by a *T-Cube DC Servo Motor Controller*. Shifting along the z axis gets an accuracy of 29 *nm*, and a maximun range of 12 *mm*. The displacement in the x-y plane is controlled by a piezoelectric controller (*piezo P-611.XZ*) moving the sample holder. Translation along the x and the y axis is achieved with a minimum accuracy of 2 *nm*.

---

[6] Thorlabs Z812B - Motorized Actuator” [28]

(working in closed-loop and with a SGS sensor, the maximum translation range is 100 μm).

The Piezoelectrics are controlled by the user through the software *SPM control* driven by an Hight Voltage Amplifier. In fig. 3.5 we can see the two panels which manage the piezos. Using an oscilloscope we monitor the outputs channel from the rear panel of the unit reported in fig. 3.5. The response of the piezo is linear respect with the applied voltage, in the range from 2 nm to 100 μm. The coefficient of proportionality is 10 $\mu m/V$.

- The collecting objective is screwed on a mobile base. This mechanism allows a displacement along the x, the$y$ and z with a precision of 10 μm over a range of 25 mm.

- The Aluminum mirror at the base of the Nanoscope can be tilted with two screws.

Figure 3.5: SPM control unit and Hight Voltage Amplifier

3.2.2 Samples

The technique used for the fabrication of the sample is the electron beam lithography and nano-processing techniques. We summarize the nanofabrication techniques in the appendix. We have two sample available. One was fabricated at *Nest*[7] and the second one is available from the *Lasim*[8].

Sample A: Aluminum Nanodisk

Sample A consists in a monocrystalline Sapphire (Al_2O_3,R-plane cut, dimension 10 mm x 10 mm e thickness 127 μm) substrate with nanopatterned Al disks. The Sapphire is a transparent dielectric, index of rifraction $n = 1.77$ @ 780 nm and $n = 1.74$ @ 1560 nm [30]. The conductibility $k = 20\ W/m \cdot K$ @ $300K$. The properties of transparency and thermal conductivity allow us to consider the Sapphire almost isothermal during the nanodisk/substrate exchange of heath. Al markers have been evaporated on the substrate top. The nominal thickness of the nanostructure is 30nm.

The sample consist of many different zones, each corresponding to different disk's dimensions. Every zone have a rectangular blade 50 μm x 0.5 mm which serves as knife-edge. Figure 3.6 reports images acquired by an optical microscope at two different magnifications. We can clearly see the knife-edge and geometric structure. These structures indicate dimension and periodicity of the disk's array. The task of this marker is to allow us to select the zone with certain specifications. Nanodisks are arranged on a rectangular periodic pattern with a minimum periodicity of $5\mu m$ up to $20\mu m$ in steps of $5\mu m$.

Thanks to the legend located at the right of the knife-edge we choose the dimension of the disk and the periodicity of the array. The disks are not visible in fig. 3.6.

Sample B:Gold/Ti Nanodisks

The second sample shows a structure similar to the previous one. In this case we have gold nanodisk evaporated on Sapphire substrate. A Titanium adhesion layer is inter-

---

[7] National Enterprise for nanoScience and nanoTechnology, Pisa, Italy

[8] Laboratoire de Spectrométrie Ionique et Moléculaire, Lyon, France

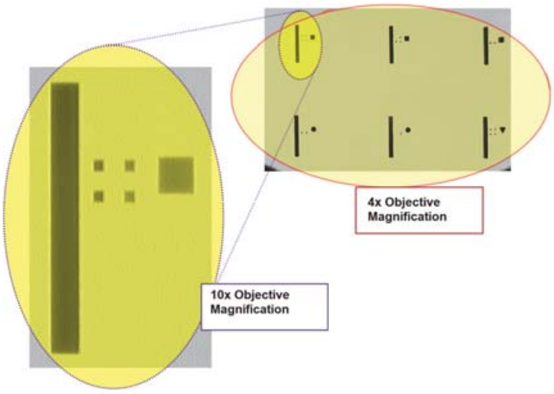

Figure 3.6: Optical images of the sample A at different magnifications.

posed. Figure 3.7 reports the thickness and the geometry. There are four sizes for the disk's diameter: 60, 70, 80, 90 and 100nm. These sizes are found in different areas and diversified according to the e-beam dose[9] adopted for e-beam lithography. A typical area of given disk diameter and dose is reported in figure 3.8 and consist of 16 nanodisks surrounded by rectangular markers.

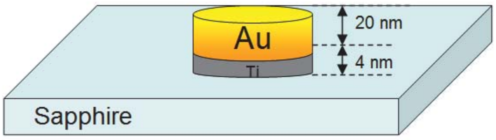

Figure 3.7: Geometry and thickness of disk of sample B.

---

[9] The dose consist in the value of exposition to electron beam

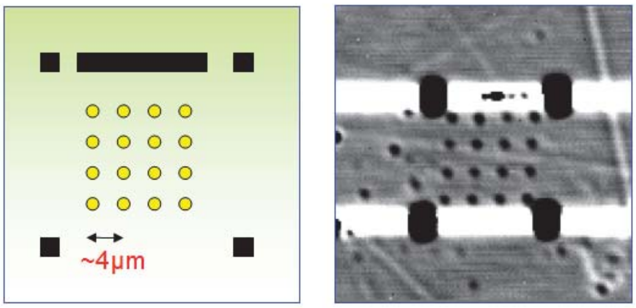

Figure 3.8: On the left is illustrated the geometry of a single exposition zone. On the right we can see an optical scanning image of size $30x30\mu m$, disk size = $100nm$ and maximum dose.

3.3 Operating procedures for the setup's setting

In this section we summarize the preliminary procedures to perform measurements by means of the Nanoscope. The detailed description is reported in the appendix, chapter "Nanoscope". The first steps describe the arrangement of the beams, the latter deal with the setting of the Nanoscope.

- **Alignment of the beams**: Laser beams must enter the Nanoscope collinearly and spatially overlapped, pump and probe measurement requires spatial coincidence of the beams. The procedure "Alignment of the beams" explains how to achieve the goal.

- **Nanoscope's Optimization**: The heart of the Nanoscope consists of two $50x$ Objective. Their first task is to focus the two beams on the sample's plane: The second is to collect them and drive them out from the Nanoscope. The instrument allows different regulations but there are two rules to respect. The two objectives must be collinear and their points must overlap. Once we get the correct setting for the objectives, the work condition is set by the height z at which we find the minimum waist[10] of the 780 beams.

---

[10] In the next sections we will discuss this term in detail

- **Reaserch of the minimum waist** The optimal condition to perform the measurement is to position the sample at the minimum waist of the probe beam. The first method to find the minimum waist relays on a manual procedure described in detail in the appendix. A more sophisticated approach will be explained after the introduction of Gaussian beam theory.

3.4 Sample and Beam imaging

When we place an object under the probe beam, we can perform two kinds of imaging. A) *sample imaging* when the object's dimension exceeds the beam's one. B) *beam imaging* in the opposite situation.

Raster scan and sample imaging

SPM control is a software which controls the displacement of the sample holder along the x and y direction, (range from 2 nm to $100\mu m$). Let's consider how to perform an imaging of a square area. Thanks to a command, namely *raster scan*, the SPM software runs a set of translation in the xy plane. These displacement follow a precise path, while the photodiode records the transmitted optical power at each point of the raster scan. The photodiode output voltage defines the greyscale of each single pixel that creates the image. We outline that the greyscale that composing the image depends on the Data Acquisition System[11]. The maximum voltage value defines the scale on which the total number of grey are assigned. Approximately 65000 gradations are available (2^{16}).

When we perform a scan we get light and dark areas. Darks areas indicate that the beam does not pass. When we do a raster scan on an extended object, as knife-edge, we obtain an image similar to figure 3.9. The path illustrated is completed trough different steps. Varying the parameter called *acquisition delay time* we can set the dwell time on each point of the scan. The speed of the scan and the acquisition delay time determine the real definition of the image.

Using the motor "Thorlabs Z812B - Motorized Actuator" it's possible to realize a com-

---

[11] Our ADC is a NI PCI-6229 that owns four analog output at 16bit

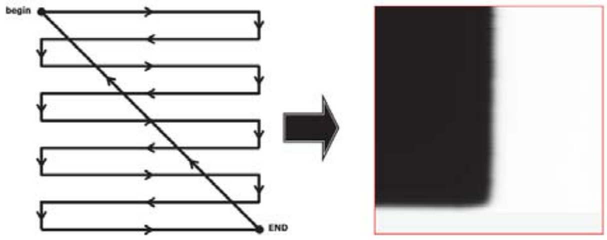

Figure 3.9: The total displacement realized by a raster scan. We can see an example of imaging obtained scanning one side of the knife-edge. The dimension of the window are 30 x 30μm, the risolution is 128 x 128 pixel.

posed movement. While the raster scan moves on the xy plane, then the motor shift the scanning plane at a different z coordinate. along the z direction. The process is called *multi raster scan*. Once we set the starting level z_i and final z_f and number of steps N, the system perform the multi raster scan. Thanks to this mechanism we are able to characterize the beam 3D intensity profile.

3.5 The Beam analysys

We now recall the basics of Gaussian beams theory. Gaussian beam theory applies provided the paraxial approximation is valid. In the second part we report the fitting functions that we use to extimate the beam waist.

3.5.1 Gaussian Beams

The Electric field of a **Gaussian beam** wich propagates alog the z direction can be mathematically represented as [31]:

$$E(r,z) = E_0 \, \frac{w_0}{w(z)} \, e^{-\frac{r^2}{w(z)^2}} \, e^{i(kz-\omega t)} \, e^{-i\zeta(z)} \, e^{\frac{ikr^2}{2R(z)}},$$

$r = \sqrt{x^2+y^2}$ stands for the radial distance from the central axis of the beam, while z indicates the axial distance from $z = 0$ (heght where beam's diameter is less).

E_0 is a costant which represents the filed's amplitude at the *minimum*.

$\frac{w_0}{w(z)}$ is a multiplicative factor which shows that the amplitude decrease with respect the beam enlargement.

$e^{-r^2/w(z)^2}$ stays for the Gaussian profile.

$e^{i(kz-\omega t)}$ indicates that the wave propagates to the positive of z.

$e^{-i\zeta(z)}$ is the phase factor that changes with respect z.

$e^{ikr^2/2R(z)}$ defines the waves front as spherical.

The corrisponding intensity distribution is :

$$I(r,z) = I_0 \, \frac{w_0^2}{w(z)^2} \, e^{-\frac{2r^2}{w(z)^2}}. \tag{3.8}$$

If the beam doesn't propagate in the air, but in an optical medium, we must consider that the wavelength is $\frac{\lambda}{n}$. The parameter $w(z)$ represents the radial distance from the z axis at which the field's amplitude is reduced by a factor $1/e$ (and intensity by a factor $1/e^2$). That term is defined *waist* while w_0 represents the **minimum waist**[12] and obeys the equation:

$$w(z) = w_0 \sqrt{\left(1 + \frac{z^2}{z_R^2}\right)}, \tag{3.9}$$

z_R is called *Rayleigh range* and defined by :

$$z_R = \frac{\pi w_0^2 n}{\lambda}. \tag{3.10}$$

If $z = \pm z_R$ the waist $w(z)$ increases by a factor $\sqrt{2}$ with respect to the minimum.

As we have already noted, w_0 represents the minimum waist of the beam. When we refer to the beam *diameter*, we mean the lenght $2w_0$. Different definitions are present, so for clarity we group them in a scheme (Figure 3.11).

The radious of curvature of the wave front $R(z)$ is:

$$R(z) = z + \frac{z_R^2}{z},$$

while the phase $\zeta(z)$ (Guoy phase) takes the form:

$$\zeta(z) = \arctan{(z/z_R)}.$$

---

[12] w_0 is an important quantity because gives us the minimum size we can get in a Gaussian beam.

The Phase $\zeta(z)$ indicates that in the passage through the focus the Gaussian beam changes its phase of a factor π in addition to the phase shift of a plane wave e^{-ikz}.

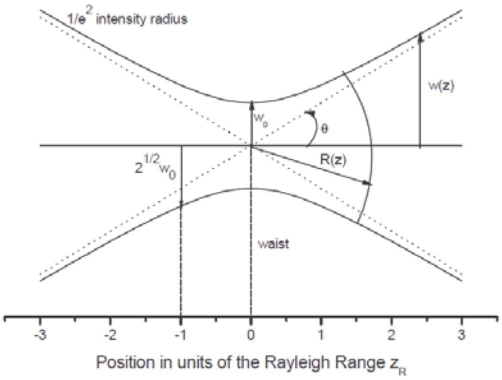

Figure 3.10: Gaussian beam intensity profile in $2D$, with respect to the propagation direction z. Main terms are indicated.

Figure 3.10 reports the intensity profile of a Gaussian beam with the waist w_0 is centered at the point $z = 0$. As we can notice far from w_0 the beam divergence is linear with respect to z. The asymptotes define the radial distance at which the intensity of the far field is reduced by a factor $1/e^2$, and are defined of:

$$\lim_{z\to\infty} w(z) = \frac{w_0}{z_R} z = \frac{\lambda}{\pi w_0 n} z \tag{3.11}$$

with respect to z, it define a limit angle θ:

$$\tan(\theta) = \lim_{z\to\infty} \frac{w(z)}{z} = \frac{\lambda}{\pi w_0 n}. \tag{3.12}$$

so:

$$\begin{aligned} \theta &= \arctan\left(\lim_{z\to\infty} \frac{w(z)}{z}\right) \\ \theta &= \frac{\lambda}{\pi w_0} \end{aligned} \tag{3.13}$$

The paraxial approximation coincides with taking small angles θ, the typical limit value is $\theta = 30$. For such angle, the tangent coincides with the argument with a precision of two decimal places. From the equation 3.13 we get the condition $w_0 \geq \frac{6\lambda}{\pi^2} \sim \frac{2\lambda}{\pi}$. The term $w_0\theta$ is defined BPP(Beam parameter product),it gives us the 'Gaussianity' of the beam. The M^2 factor is expressed by:

$$M^2 = \frac{BPP_{sp}}{BPP_{th}}.$$

M^2 tells us how the real beam differs from the ideal case.
It holds that:
$M^2 = 1$ for an ideal Gaussian beam
$M^2 > 1$ for a real Gaussian beam The higher the value is, the more the beam differs from the ideal case.

Considering a real beam propagating in a medium with an index of refraction n:

$$(w_0\theta)_{sp} = \frac{\lambda}{\pi n} M^2 \tag{3.14}$$

and the *Rayleigh range* becomes:

$$z_{R,sp} = \frac{\pi w_0^2 n}{\lambda M^2}. \tag{3.15}$$

The equation of the intensity is:

$$I(r,z)_{sp} = \frac{I_0}{1 + \left(\frac{\lambda M^2 z}{\pi w_0^2 n}\right)^2} \quad exp\left[-\frac{2r^2}{w_0^2\left[1 + \left(\frac{\lambda M^2 z}{\pi w_0^2 n}\right)^2\right]}\right], \tag{3.16}$$

while the radius equation is $w(z)$:

$$w(z) = w_0\sqrt{\left(1 + \frac{(M^2)^2 z^2}{z_R^2}\right)}. \tag{3.17}$$

Beam's dimension and notation

This thesis adopts the parameter $w(z)$ to describe the half width of the Gaussian beam. For the intensity, $w(z)$ is the distance from the central axis where the height of the Gaussian distribution is equal to $1/e^2$ of the maximum value. Because we are cutting off a distribution which tends to 0 at the infinity, the choice is arbitrary. When we describe the intensity with a Gaussian distribution in that form:

$$I(x,z) = I_0 e^{-\frac{x^2}{2\sigma(z)^2}} \tag{3.18}$$

there exist other two other common choices, the standard deviation end the *FWHM*.[13]. From the comparison of equation 3.8 and 3.18, we get:

$$w = 2\sigma$$

and

$$w = \frac{FWHM}{\sqrt{2\ln 2}}.$$

In order to characterize the *pump* and *probe*'s beam we realize an estimate of the minimum waists, that we define $w_{0,s}$ and $w_{0,p}$. The dimension of w_0 is fundamental to calculate the energy transferred per unit area and to estimate the amount of energy tranferred to the sample.

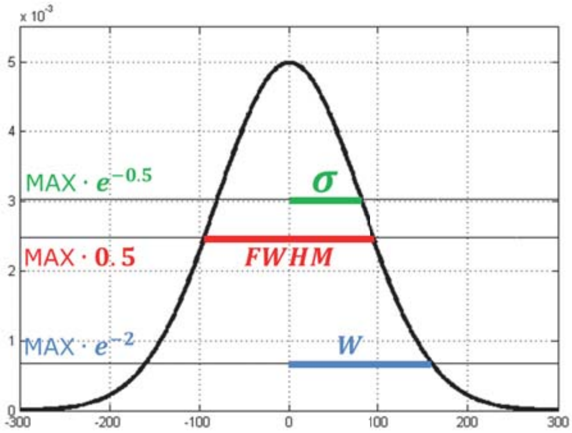

Figure 3.11: Comparison between parameters σ, $FWHM$ and w of a Gaussian distribution.

---

[13] Full width at half maximum

3.5.2 Experimental analysis of the laser beam

The operative procedure that we use to characterize the beam is as follows. An automated procedure perform a raster scan at different heights z. Every raster scan gives an image of a side of the knife-edge which consists in a matrix of data. Every line of the raster, pictured in figure 3.9, gives an array of voltage. Let's consider the 1 D case. If we acquire a single line of the raster we obtain a graph with a sigmoid profile. The movement of the blade and the sigmoid curve are reported in Fig. 3.12.

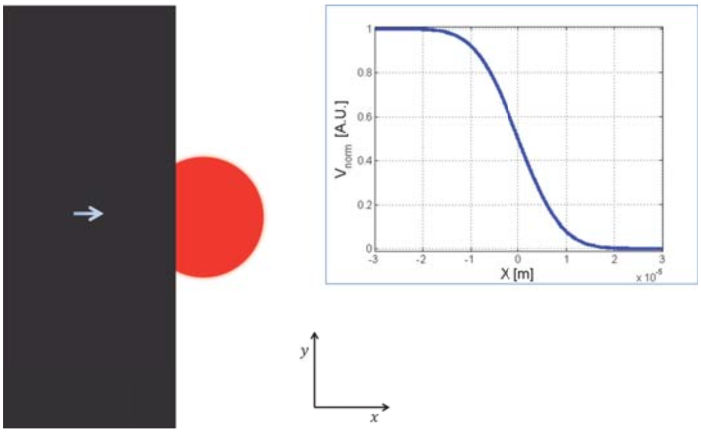

Figure 3.12: What happens and what we measure. A *sigmoid curve* $Voltage$ VS x is produced at every entry of the edge. The curve is normalized.

Now we need a function to fit the *sigmoid* curve. Assuming that our beam propagates along z direction[14] and has got a Gaussian profile of intensity:

$$I(x,y) = I_0 \; e^{-2x^2/w_x^2} \; e^{-2y^2/w_y^2}$$

I_0 is the maximum intensity, while w_x e w_y are the beam's waist (at $1/e^2$) along x and y direction. Translating the knife-edge along the x direction, as shown in figure 3.12, we get the trasmitted power :

$$P(X) = P_{TOT} - I_0 \int_{-\infty}^{X} e^{-2x^2/w_x^2} \, dx \int_{-\infty}^{\infty} e^{-2y^2/w_y^2} \, dy.$$

---

[14] Opposite to the direction indicated in Fig.3.4

Using the standard definition of Error function, we get the expression:

$$P(X) = \frac{P_{TOT}}{2}\left[1 - erf\left(\frac{\sqrt{2}X}{w_x}\right)\right]. \tag{3.19}$$

With equation 3.19 we can fit every sigmoid curve V versus x. It's convenient to whrite it as:

$$P(X) = \frac{P_{TOT}}{2}\left[1 \pm erf\left(\frac{\sqrt{2}\,(X - X_0)}{w_x}\right)\right]. \tag{3.20}$$

where w_x corresponds to the Gaussian beam's radius (at $1/e^2$) and signum - (+) is chosen when the edge translates along the positive or the negative direction. Using the equation 3.20 as fitting function, we get a value of waist for each raster scan. If the beam has a Gaussian profile, we can fit points using equation 3.9 in the form:

$$w(z) = w_0\sqrt{\left(1 + \frac{(z - z_0)^2}{z_R^2}\right)}, \tag{3.21}$$

where z_0 corresponds to the height of minimum waist of *probe* beam.

If we want to consider the non ideal beam, equation 3.21 is modified to :

$$w(z) = w_0\sqrt{\left(1 + \frac{(M^2)^2(z - z_0)^2}{z_R^2}\right)}. \tag{3.22}$$

where w_0 corresponds to the minimum waist of *probe* beam, while M^2 is a number greater than 1. The procedure illustrated is general and suitable for both pump and probe beams. We obtain of $w_(z)$ in function of z. Furthermore, we can get values of *minimum waist* w_0. Nevertheless, it is possible to use a faster method in order to estimate the same results. This procedure is called 90-100 *method* however we adoperate the first method exposed.

3.5.3 Graphs and curve fitting

Before showing the experimental result we must make a clarification. The Sapphire substrate is transparent and allows to place the sample on the sample holder in two different ways. In figure 3.13 are shown the upright and the inverted case. The main difference is that the beam, when cut from the knife-edge, comes from one of different index of refraction. The developed theory assumes that the index of refraction is uniform.

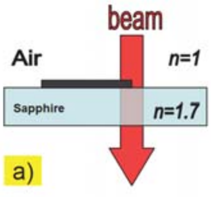

Figure 3.13: Two possible configurations of mounting the sample. In case a) knife-edge cuts the beam before crossing the substrate of sapphire. In case b) the two actions are reversed. Za means Sapphire

For that reason the experimental points obtained with the sample in case b) cannot be fitted.

Let's report the first plot in figure 3.14. The orange points stand for the probe's waist values and are labelled as w_s. Blue points represent the values of the pump's beam waist w_p with respect to the height z. Each point was obtained using the acquisition procedure described previously. Observing the relative height z, we note that the point

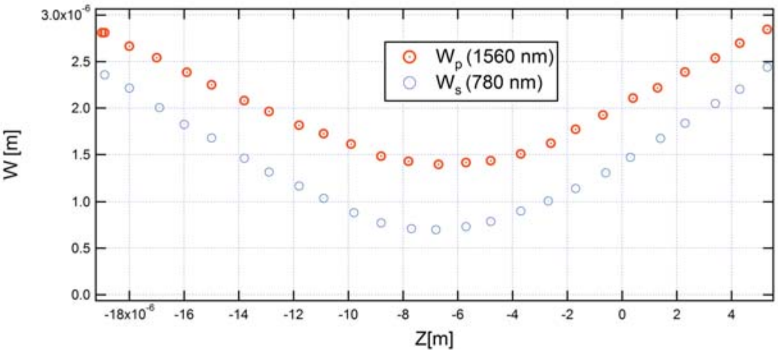

Figure 3.14: Plot of $w(z)$ for the pump and probe beam. The wavelengths of the two beams are indicated. Each value of waist has been obtained through a "rasterscan" of $40x40\mu$m and a $128x128$ pixel resolution

z_0 of the minimum waist w_0 is different for the two beams. Such effect is due to chromatic aberration. The probe waist w_s reaches lower values, in the present it was $0.7\mu m$. The pump's minimum waist is about $1,4\mu m$. Since the sample was presumibly mounted as in case b) of figure 3.13, we can't fit these points using Equation 3.21. Besides we notice that the minimum waist w_0 assumes a value that is lower than typically obtained in the present thesis.[15]. We impute this fact to the higher index of refraction of the Sapphire[16]. The divergence of the two beams looks different, that's due to their wave lengths. The probe's divergence is higher than the pump's one.

Once we upside the sample, we acquired a multiscan to characterize the probe beam. Figure 3.15 reports the result and shows the fit function. The points have been fitted with $n = 1$. In table 3.1 are indicated the coefficients w_0, z_0 and M^2 obtained by means of the fit process.

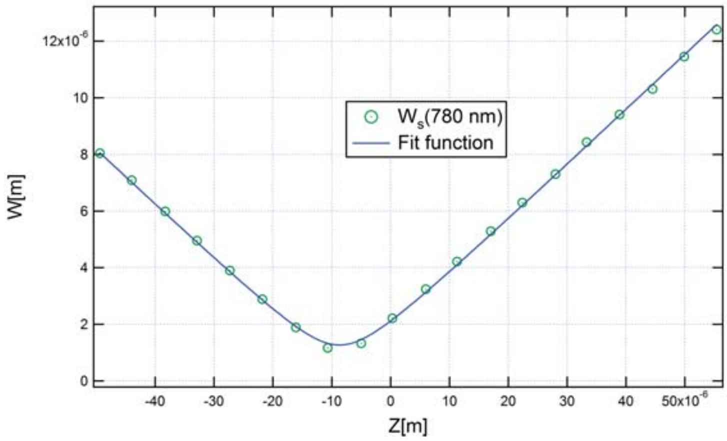

Figure 3.15: Fit of of $w(z)$ in function of z for the probe beam.

3.5.4 Energy density per pulse

The waist $w(z)$ allows to calculate a key quantity: the energy density of the beam. Pump and probe's measurements require estimating the energy ceded to the sample. By

---

[15] Typical value of waist w_0 for the probe beam are $\sim 1\mu m$. We never obtained the minimum theoretical value $\sim 0.63\lambda$

[16] n=1.76

	Quantities	Value $[m]$	Error $[m]$
780 nm	w_0	$1.27 \cdot 10^{-6}$	$6.2 \cdot 10^{-8}$
	z_0	$-8.67 \cdot 10^{-5}$	$1.4 \cdot 10^{-7}$
	M^2	1	0.04
	$n(fixed)$	1	0

Table 3.1: Fit coefficients relative to figure 3.15 with absolute errors.

means of a power meter we measure the power of the two beams after they enter the Nanoscope. If we consider that some energy is lost at every mirror reflection, we can estimate the average power which impacts on the sample. Let's evaluate the energy per pulse of the two beams per unit area. The current values of average power which impact on the sample are[17] :

$$P_{probe} = 5.64 \cdot 10^{-4} W$$

$$P_{pump} = 3.76 \cdot 10^{-2} W$$

The *repetition rate* of the laser's cavities is $\nu = 10^{-}8Hz$. Hence the energy per pulse is :

$$P_{beam} \cdot 10^{-8} sec$$

. The energy valueper pulse per unit area is defined by the ratio:

$$\frac{dE}{dS} = \frac{P \cdot 10^{-8} s}{\pi w^2}. \tag{3.23}$$

The working condition is realized when the sample holder is placed at a z_0 height. Hence we assume that the probe's beam diameter is w_0. From the values listed in table 3.1 for

---

[17] We measured beam's power through a power meter placed at the entry of the nanoscope. We considered a total loss due to mirrors of 0.06%.

the *probe* we get:

$$\left.\frac{dE}{dS}\right|_{z_0} = 1.2\ J/m^2,$$

and if we consider a $w_p = 1.6\mu m$, for the *pump*, we obtain:

$$\left.\frac{dE}{dS}\right|_{z_0} = 46.7\ J/m^2.$$

Chapter 4

Spatial Modulation Imaging

In this chapter we introduce and explain the Spatial Modulation Spectroscopy. This work was done in collaboration with Fabio Medeghini who contributed with his bachelor thesis work. In the first part we introduce the technique. In the second part we report the experimental setup and results performed on a single nanodisks.

4.1 Why spatial modulation spectroscopy?

Optical techniques are powerful instruments to study and characterize nanomaterials. These techniques can investigate the optical properties of a nano-object which are related to its volume and composition to the surrounding material. Being able to work on a single nanoparticle, instead than on a nanoparticles ensemble, is essential to get accurate information on the single object properties. This is the reason why the studies of individual nano-objects are nowadays widespread.

The detection of a single nanoparticle can be achieved by the use of far-field techniques. The advantages of these techniques are the easy interpretations of the data (avoiding sample-tip interaction a major problem occurring in near field techniques). However the resolution is limited by the diffraction limit of the light (resolution $\sim \lambda$ in a focalized beam), that bind to utilize diluted samples. Far-field techniques, as the one object of the present work, are based on the detection of the absorbed or scattered component of the incident beam. The scattering decreases strongly with respect to the dimension of

the particle ($\sim V^2$), while the absorption has a slower dependence ($\sim V$).
Here we implement a technique first developed by Del Fatti and Vallée group [?] Exploiting a spatial modulation of the nanoparticle we can measure the extinction of the incident beam. In this way a single nano object can be localized and analyzed. These measurements allow, in same cases, to obtain dimensions, shape and orientation of an object way smaller than the wave length λ [20].

The experimental equipment consists in a laser light source, collimated by two identical microscope objectives. The first objective focalizes the incident beam on the sample, while the second one collect the transmitted beam toward a photodiode. we implemented spatial modulation nanoscopy within the nanoscope. We exploit the technique to detect the nanodisk on which pump & probe measurements will be performed. The probe beam must be centered on a disk with a precision comparable to the beam waist, or less. For that reason we needed an high accuracy in the positioning. Let's introduce the basic principle of spatial modulation imaging. The relative variation of transmitted power $\frac{P_t-P_i}{P_i}$ (P_t is the transmitted power beyond the particle, P_i is the incident power, i.e. the transmitted power without the particle)through a sample consisting of a single nanoparticle with size smaller then the beam's one is very weak. If the beam dimension is small enough, it's possible to detect small objects as a nanodisks. The limit of the "standard" detection is given by the noise. If the the variation of transmitted power is very weak, the noise can overcome the signal itself. A possible solution consists in the *spatial modulation* of the nanoparticle at a well-known frequency ν. In this way the particle oscillates inside the focalized beam with frequency ν and, by the use of a lock-in amplifier, the transmitted signal at the same frequency can be detected. The lock-in filters the noise placed out of the passing-band, centered at ν.
More in detail, the position modulation implies a modulated trasmissivity ΔT or, equally, a transmitted power modulation P_t. Referring to relative variations:

$$\frac{\Delta T}{T_i} = \frac{P_{ext}}{P_i} = \frac{P_t - P_i}{P_i},$$

where P_i is the total power of the beam, P_t stands for the transmitted power of the beam after the absorption and the scattering due to the presence of the particle. P_{ext}

denotes the extinguished power, T_i is the transmission coefficient without the particle, ΔT indicates the variation of T_i when the particle is present. The modulation of the transmitted power P_t is detected with the help of a lock-in amplifier, while the incident power P_i can be evaluated with a photo-detector (power meter).

The position modulation is realized feeding a piezoelectric placed under the sample with an oscillating tension $V(t) = V_0 \sin(2\pi\nu t)$. The sample and the piezoelectric are placed on a mobile sample holder which can be moved along the X and the Y axis. By the slow change of the sample coordinates (x_0, y_0) meanwhile the piezoelectric is oscillating one can get a cartography of sample and spot out the nanoparticle location.

This technique is called spatial modulation spectroscopy and henceforth it will be indicated with the acronym SMS.

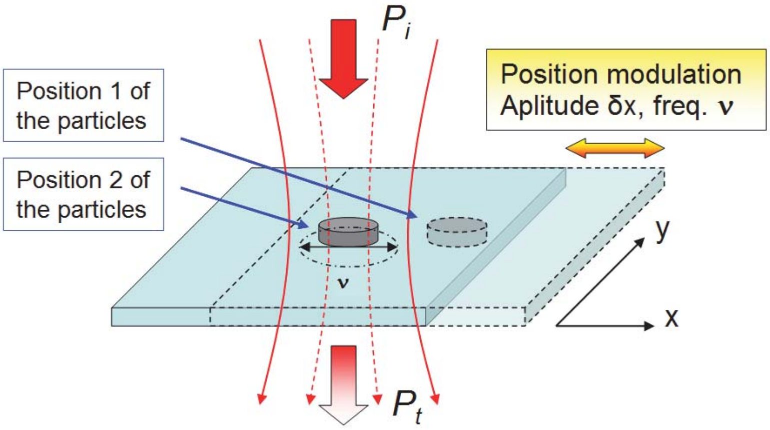

Figure 4.1: Working principle of the SMS technique.

4.2 Principle of operation

We start following the explanation given by the Lyon group [37], who first developed the SMS technique. Let's assume that at the nanoparticle's height z_0 the spacial profile of the intensity $I(x,y)$ is Gaussian-like. The intensity $I(x,y)$ has dimension $[\frac{W}{m^2}]$. Considering that the beam run into the single nanoparticle positioned at a coordinate (x_0, y_0), the transmitted power P_t can be expressed by:

$$P_t = P_i - P_{ext},$$

the extincted power, due to the particle's presence, can be written as:

$$P_{ext}(x_0, y_0) = \sigma_{ext} I(x_0, y_0), \tag{4.1}$$

where $I(x_0, y_0)$ stands for the light intensity in the point (x_0, y_0), while σ_{ext} is the extinction cross section, which is the sum of a scattering and absorption contributes: $\sigma_{ext} = \sigma_{scatt} + \sigma_{ass}$.

$I(x_0, y_0)$ is measured in $[\frac{W}{m^2}]$, while σ_{ext} in $[m^2]$.

Assuming that the nanoparticle's position is modulated with a frequency ν in the x direction and with amplitude δ_x:

$$(x(t), y(t)) = (x_0 + \delta_x \sin(2\pi\nu t), y_0)$$

the transmitted power will be modulated too:

$$P_t = P_i - \sigma_{ext} I(x_0 + \delta_x \sin(2\pi\nu t), y_0). \tag{4.2}$$

If the modulation's amplitude δ_x is way smaller than the dimension of the incident beam ($\delta_x << a$, where a is the spot diameter), P_t can be expanded in series:

$$P_t \approx P_i - \sigma_{ext} \left[I(x_0, y_0) + \delta_x \frac{\partial I}{\partial x}\bigg|_{\substack{x=x_0\\y=y_0}} \sin(2\pi\nu t) + \frac{\delta_x^2}{2} \frac{\partial^2 I}{\partial x^2}\bigg|_{\substack{x=x_0\\y=y_0}} \sin^2(2\pi\nu t) \right] \tag{4.3}$$

The last addendum can be cast in the following way:

$$\sin^2(2\pi\nu t) = \frac{1}{2} - \frac{1}{2}\cos(2\pi 2\nu t) = \frac{1}{2} - \frac{1}{2}\sin\left(\frac{\pi}{2} + 2\pi 2\nu t\right). \tag{4.4}$$

Thereby the relative variation of the transmissivity $\Delta T_t/T_i = (P_t - P_i)/P_i$ includes oscillating components at ν and at 2ν proportionals, respectively, to the first derivative and to the second derivative of the intensity $I(x,y)$ with respect to x.

Summing up the main concepts, the model is developed under three hypothesis:

1)

$$I(x,y) = A \exp\left[-\frac{(x-B)^2+(y-D)^2}{2a^2}\right]$$

The intensity $I(x,y)$ of the laser beam must have a Gaussian profile with standard deviation a. In this case the signals at ν and at 2ν will be proportionals, respectively, to the first derivative and to the second derivative of the well-known Gaussian distribution.

2)

$$r << a$$

The diameter of the extinction cross section σ_{ext} of the nanoparticle must be way smaller than the diameter d of the spot's intensity. Only under this condition Equation 4.1 is correct, otherwise the second addendum with $x = x(t)$ it should be replaced by its integral form:

$$P_{ext}(x_0, y_0) = \iint_{\sigma_{ext}} I(x,y)\, dx\, dy. \tag{4.5}$$

3)

$$\delta_x << a$$

The modulation's amplitude δ_x must be way smaller than the standard deviation a of the Gaussian profile. This statement is essential to make relevant the first elements of the series with respect to the successive ones.

If these conditions are valid, the signal detected at ν will be proportional to:

$$-\sigma_{ext}\ \delta_x\ \frac{\partial I}{\partial x}\bigg|_{\substack{x=x_0\\ y=y_0}},$$

while the signal gained at 2ν will be proportional to:

$$-\sigma_{ext}\ \frac{\delta_x^2}{4}\ \frac{\partial^2 I}{\partial x^2}\bigg|_{\substack{x=x_0\\ y=y_0}}.$$

A cartography can be realized through a scan of the sample on the xy plane. As we shall see, working with spatial modulation at the frequency ν, we obtain a signal composed of two “lobes“ (but of opposite sign). Acquiring the signal at 2ν, the signal will have its maximum at the center of the Gaussian profile. The trend of the signal acquired at ν and 2ν are shows in figure 4.2 in 1D. Those plots, however, are only proportional to the signal that we would measure.

If the oscillations are wide the hypothesis 3) fall and the previous approximation is not true anymore. In this case the transmitted power must be calculated numerically applying the Fourier transform directly on Equation 4.2. We report the numerical results calculated by [20]. Figure 4.3 shows that varing the amplitude of modulation we get a more or less sharp spatial distribution.

4.2.1 Simple explanation: 1D case

If the nanoparticle is extended hypothesis 2) falls and the second addendum in Equation 4.2 must be replaced by Equation 4.5. To give a simple explanation, let’s assume that we are in a 1D world. In one dimension the disk of radius r is substituted by a line segment of length $2r$. Specializing equation 4.5 to the 1D problem we obtain:

$$P_t(x_0) = P_i - \int_{x_0-r}^{x_0+r} I(x')\,dx', \tag{4.6}$$

where the 1D intensity profile $I(x')$ has dimensions $[\frac{W}{m}]$.

Considering the position’s modulation of the center of the disk:

$$x(t) = x_0 + \delta_x \sin(2\pi\nu t)$$

also the edges of the disk will oscillate, so:

$$P_t(x_0,t) = P_i - \int_{x(t)-r}^{x(t)+r} I(x')\,dx' = P_i - \int_{x_0+\delta_x\sin(2\pi\nu t)-r}^{x_0+\delta_x\sin(2\pi\nu t)+r} I(x')\,dx'.$$

Operating the variable change $\{x'' = x' - \delta_x \sin(2\pi\nu t)\}$ one get:

$$P_t(x_0,t) = P_i - \int_{x_0-r}^{x_0+r} I(x'' + \delta_x \sin(2\pi\nu t))\,dx''.$$

which represents the physical situation of the disk fixed in x_0 and of the beam oscillating along x with frequency ν and amplitude δ_x.

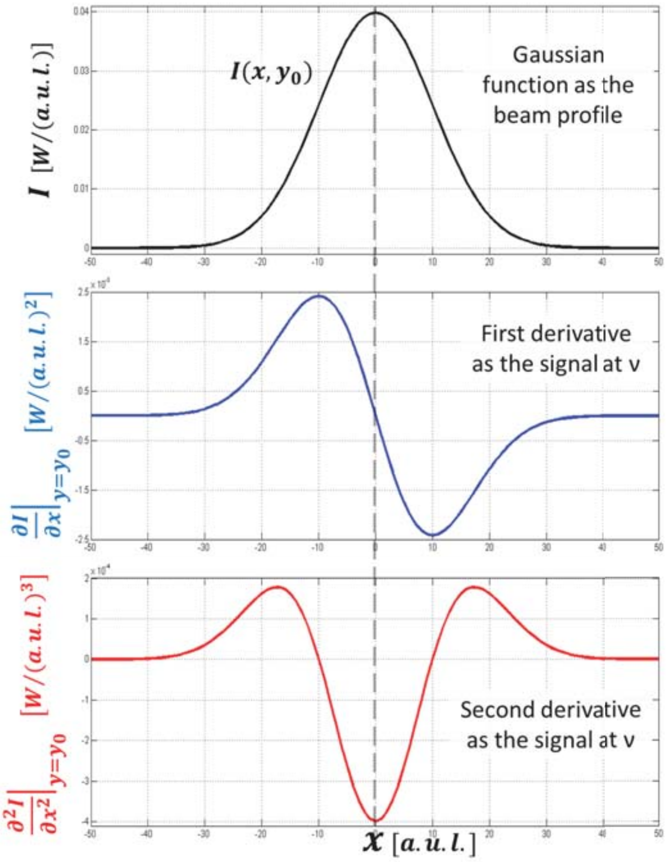

Figure 4.2: Above: plot of the 1D Gaussian distribution $I(x, y_0) = \frac{P_i}{\sqrt{2\pi}\,a} \exp\left[-\frac{x^2}{2a^2}\right]$ (with $a = 10$, $a.u.l.$ and $P_i = 1\,W$) that stands for a Gaussian intensity distribution x. Below: plots of the derivatives of the Intensity proportional to the components ν (blue curve) and at 2ν (red curve) of the intensity profiles due to a oscillating particle. These two curves are function of the average position (x_0, y_0) of the particle. The x axis is shared by the three graphics. [a.u.l] stands for arbitrary units of length.

.

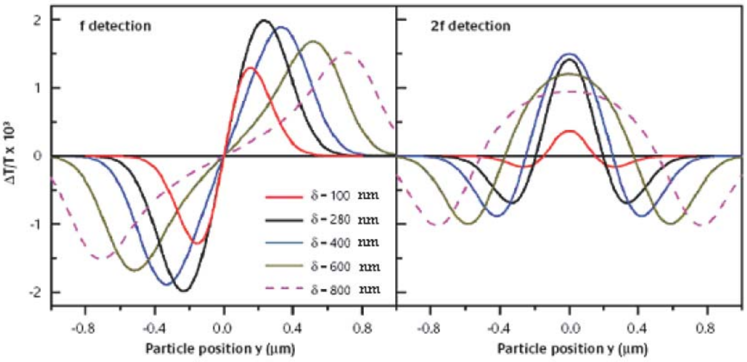

Figure 4.3: Relative variation of transmission modulated at ν and at 2ν for a Gaussian beam centered in (x_0, y_0); the signal is given by the extinction of a nanoparticle with cross section $\sigma_{ext} = 290nm^2$. The position of the particle is modulated along the y direction. The curves have been calculated for several amplitude of modulation, respectively $100nm$, $280nm$, $400nm$, $600nm$, $800nm$. Taken from [20]

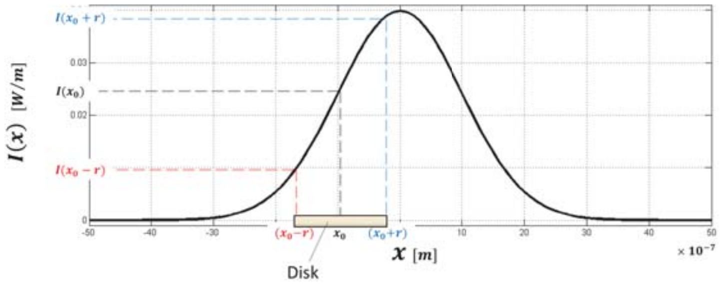

Figure 4.4: In a one dimension a disk of radius r is a segment of length 2r, centered in x_0.

Under the hypothesis 3) of little oscillations ($\delta_x << a$), the series expansion can made:

$$I(x'' + \delta_x \sin(2\pi\nu t)) \approx I(x'') + \delta_x \left.\frac{\partial I}{\partial x}\right|_{x=x''} \sin(2\pi\nu t) + \frac{\delta_x^2}{2} \left.\frac{\partial^2 I}{\partial x^2}\right|_{x=x''} \sin^2(2\pi\nu t).$$

It follows:

$$\begin{aligned} P_t(x_0, t) = P_i - &\left[\int_{x_0-r}^{x_0+r} I(x'')\ dx''\right] + \left[\int_{x_0-r}^{x_0+r} \delta_x \left.\frac{\partial I}{\partial x}\right|_{x=x''}\right] \sin(2\pi\nu t)\ dx'' \\ &+ \left[\int_{x_0-r}^{x_0+r} \frac{\delta_x^2}{2} \left.\frac{\partial^2 I}{\partial x^2}\right|_{x=x''}\right] \sin^2(2\pi\nu t)\ dx' \end{aligned}$$

The signal detected at ν will be proportional to:

$$-\delta_x \ \left[I(x_0 + r) - I(x_0 - r)\right], \tag{4.7}$$

while, with the help pf Equation 4.4, the signal detected at 2ν will be proportional to:

$$-\frac{\delta_x^2}{4} \left[\left.\frac{\partial I}{\partial x}\right|_{x=x_0+r} - \left.\frac{\partial I}{\partial x}\right|_{x=x_0-r}\right]. \tag{4.8}$$

Under the hypothesis 1) is true the intensity profile $I(x)$ is Gaussian shaped with standard deviation a. We consider, for sake of making an example, a normalized Gaussian function

$$I(x) = \frac{P_i}{\sqrt{2\pi}a} \exp\left[-\frac{x^2}{2a^2}\right]$$

with $a = 1\mu m$ and P_i (for a normalized Gaussian function is meant:

$$\int_{-\infty}^{+\infty} I(x)\ dx = P_i$$

and show the expected signals at ν and at 2ν on varying the radius r.

In Figure 4.5 are reported the signals at ν (above) and at 2ν (below) for several values of the radius r. These signals have been calculated using Equations 4.7 and 4.8. With increasing r, the signal spatial distributions become larger and less sharp reducing the spacial resolution. Focusing on the borderline cases, it is clear that for small radiuses the signals get back to the Gaussian derivatives. On the other extreme if we consider a big radius the signals become what one would expect modulating a knife-edge under a focused beam.

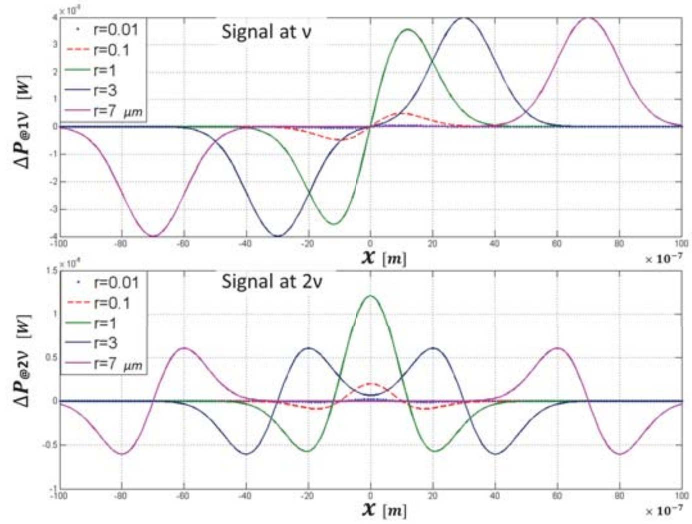

Figure 4.5: Signals at ν and at 2ν calculated considering a Gaussian beam with $a = 1\mu m$, power $P_i = 1\,W$, a modulation amplitude $\delta_x = 0.01\mu m$ and a radius r of 0.01, 0.1, 1, 3 and $7\mu m$.

Since the signals obtained modulating with small radiuses have a very low magnitude, it is useful to compare normalized signals.

The normalized curves of Figure 4.5 are reported in the graphics of Figure 4.6. Here the black curves correspond to the first derivative (above) and to the second one (below) of the Gaussian distribution of Figure 4.4. As one can see, for small values of radiuses r, where the condition $r << a$ is met ($r = 0.01\mu m$, $r = 0.1\mu m$), the signals follow the Gaussian derivatives.

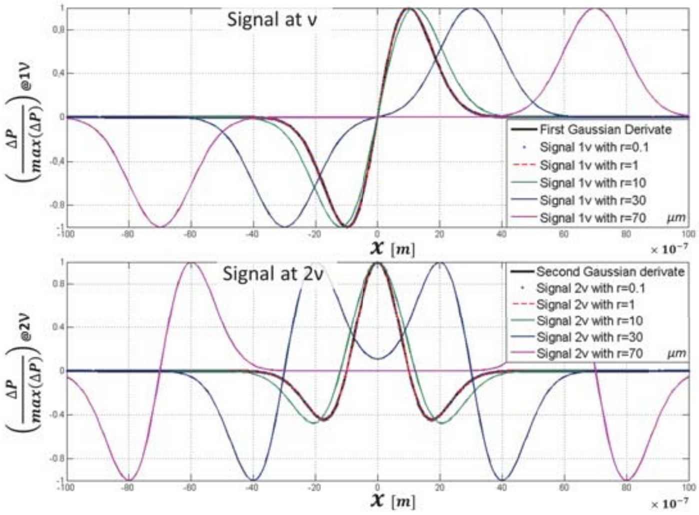

Figure 4.6: Signals at ν and at 2ν normalized to their maximum value and calculated considering a Gaussian beam with $a = 1\mu m$, power $P_i = 1\,W$, a modulation amplitude of $\delta_x = 0.01\mu m$ and a radius r of 0.01, 0.1, 1, 3 and $7\mu m$. The black curves are the normalized Gaussian derivatives of the Gaussian distribution with $a = 1\mu m$. The normalized signals with $r = 0.01\mu m$ and $r = 0.1\mu m$ and the normalized Gaussian derivatives are overlapping.

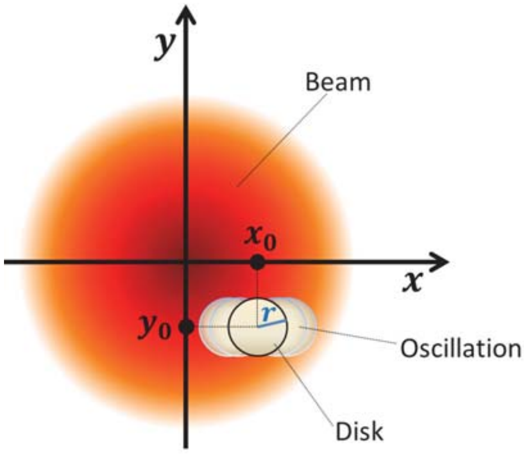

Figure 4.7: Bird's-eye view. Cross section as an extended disk of radius r oscillating along the x direction with amplitude δ_x and frequency ν. The red circle stand for the spot of the beam on the sample plane.

4.2.2 The real case : 2D case

Extending the reasoning of the 1D case to the real 2D case of a cylindrical particle of "disk area" $\sigma_{ext} = \pi r^2$, one obtains, modifying the second addendum in Equation 4.6:

$$P_{ext}(x_0, y_0) = \iint_{disk} I(x,y)\, dx\, dy,$$

Where the intensity $I(x,y)$ dimensions $[\frac{W}{m^2}]$ is taken as a Gaussian function with standard deviation a, P_i being the incident power:

$$I(x,y) = \frac{P_i}{2\pi a^2} \exp\left[-\frac{x^2+y^2}{2a^2}\right].$$

(The normalization of the Gaussian function implies $\int_{-\infty}^{+\infty}\int_{-\infty}^{+\infty} I(x,y)\, dx\, dy = P_i$).

The equation of the circumference of radius r centered in (x_0, y_0) is:

$(x - x_0)^2 + (y - y_0)^2 = r^2$, hence:

$$\begin{aligned} P_t(x_0, y_0) = P_i - & \int_{y_0-r}^{y_0+r} \int_{x_0}^{x_0+\sqrt{r^2-(y'-y_0)^2}} I(x', y')\, dx'\, dy' \\ - & \int_{y_0-r}^{y_0+r} \int_{x_0}^{x_0-\sqrt{r^2-(y'-y_0)^2}} I(x', y')\, dx'\, dy'. \end{aligned}$$

On the other hand the position's modulation is still complemented along the x direction only:

$$(x(t), y(t)) = (x_0 + \delta_x \sin(2\pi\nu t), y_0),$$

Therefore we obtain:

$$\begin{aligned} P_t(x_0, y_0, t) = P_i - & \int_{y_0-r}^{y_0+r} \int_{x_0+\delta_x \sin(2\pi\nu t)}^{x_0+\delta_x \sin(2\pi\nu t)+\sqrt{r^2-(y'-y_0)^2}} I(x', y')\, dx'\, dy' \\ - & \int_{y_0-r}^{y_0+r} \int_{x_0+\delta_x \sin(2\pi\nu t)}^{x_0+\delta_x \sin(2\pi\nu t)-\sqrt{r^2-(y'-y_0)^2}} I(x', y')\, dx'\, dy', \end{aligned}$$

that, under the usual variable change $\{x'' = x' - \delta_x \sin(2\pi\nu t), y'' = y'\}$, becomes:

$$\begin{aligned} P_t(x_0, y_0, t) = P_i - & \int_{y_0-r}^{y_0+r} \int_{x_0}^{x_0+\sqrt{r^2-(y''-y_0)^2}} I\big(x'' + \delta_x \sin(2\pi\nu t), y''\big)\, dx''\, dy'' \\ - & \int_{y_0-r}^{y_0+r} \int_{x_0}^{x_0-\sqrt{r^2-(y''-y_0)^2}} I\big(x'' + \delta_x \sin(2\pi\nu t), y''\big)\, dx''\, dy''. \end{aligned}$$

Under small oscillations ($\delta_x << a$), on the approximation:

$$I\big(x'' + \delta_x \sin(2\pi\nu t), y''\big) \approx I(x'', y'') + \delta_x \frac{\partial I}{\partial x}\bigg|_{\substack{x=x'' \\ y=y''}} \sin(2\pi\nu t) + \frac{\delta_x^2}{2} \frac{\partial^2 I}{\partial x^2}\bigg|_{\substack{x=x'' \\ y=y''}} \sin^2(2\pi\nu t).$$

From Equation 4.4 it follows:

$$\begin{aligned} P_t(x_0, y_0, t) = P_i - & \left[\iint_{disk} \left(I(x'', y'') + \frac{\delta_x^2}{4} \frac{\partial^2 I}{\partial x^2}\bigg|_{\substack{x=x'' \\ y=y''}} \right) dx''\, dy'' \right] \\ - & \left[\iint_{disk} \left(\delta_x \frac{\partial I}{\partial x}\bigg|_{\substack{x=x'' \\ y=y''}} \right) dx''\, dy'' \right] \cdot \ \sin(2\pi\nu t) \\ + & \left[\iint_{disk} \left(\frac{\delta_x^2}{4} \frac{\partial^2 I}{\partial x^2}\bigg|_{\substack{x=x'' \\ y=y''}} \right) dx''\, dy'' \right] \cdot \ \sin(\frac{\pi}{2} + 2\pi 2\nu t)\ . \end{aligned} \tag{4.9}$$

Therefore the signal detected at ν will be proportional to:

$$- \left[\iint_{disk} \left(\delta_x \frac{\partial I}{\partial x}\bigg|_{\substack{x=x'' \\ y=y''}} \right) dx''\, dy'' \right], \tag{4.10}$$

while the signal detected at 2ν will be proportional to:

$$-\left[\iint\limits_{disk}\left(\frac{\delta_x^2}{4}\frac{\partial^2 I}{\partial x^2}\bigg|_{\substack{x=x''\\y=y''}}\right)dx''\,dy''\right]. \tag{4.11}$$

These expressions are not easy to evaluate analytically. Nevertheless the numerical approach is relatively simple, we assume that: the intensity distribution is a Gaussian, and we assume that the cross section of the disk can be reduced to the disk's circle surface[1] The derivatives of $I(x,y)$ are calculated analytically, the numerics — to the integral over the circular domain.

Several numerical simulations have been done varying the parameters: a, r, δ_x and Δx. This last parameter Δx has been introduced to state the length in meters of the side of the unit cell $\Delta x \Delta y$ used to discretized the two dimensional space xy. Supposing that $\Delta x \Delta y$ is squared, it follows: $\Delta x = \Delta y$. Experimentally Δx indicates the amplitude of the translation produced by the piezoelectric to position the disk from the origin (x_0, y_0) to the origin $(x_0 + \Delta x, y_0)$. In fact, a signal is acquired only throughout an oscillation on a fixed site. As said previously, these translations between origins are essential to realize a cartography. Summarizing a is the standard deviation of the Gaussian distribution, r specifies the radius of the cross section that, for the present calculations, correspond to the radius of the physical disk, δ_x is the spacial modulation's amplitude and, for hypothesis, must be way smaller than a.

---

[1] This is a very strong position in thus is tacitly disregard: 1) scattering effect, 2) total absorption of the e.m. radiation with k_z vectors ending on the disk. Basically is a geometrical optics approximation treating the disk as fully absorbing.

We now estimate the relative intensities of the signals acquired at ν and 2ν. To this end it is useful to consider the quantities A and B, that are, respectively, the maximum of the signal at ν and of the signal at 2ν:

$$A = \max\left\{ \left| \iint\limits_{disk} \left(\delta_x \frac{\partial I}{\partial x}\bigg|_{\substack{x=x'' \\ y=y''}} \right) dx''\, dy'' \right| \right\}, \tag{4.12}$$

$$B = \max\left\{ \left| \iint\limits_{disk} \left(\frac{\delta_x^2}{4} \frac{\partial^2 I}{\partial x^2}\bigg|_{\substack{x=x'' \\ y=y''}} \right) dx''\, dy'' \right| \right\}. \tag{4.13}$$

In table 4.1 the values of the coefficients used in some numerical simulations reported. The total incident power is taken as 1 Watt: $P_i = 1\,W$.

a	δ_x	Δx	r	A	B	A/B
$[m]$	$[m]$	$[m]$	$[m]$	$[W]$	$[W]$	
10^{-6}	10^{-8}	10^{-7}	10^{-7}	$1.9 \cdot 10^{-5}$	$7.9 \cdot 10^{-8}$	243
		10^{-7}	$4 \cdot 10^{-7}$	$4.4 \cdot 10^{-4}$	$1.8 \cdot 10^{-6}$	248
		10^{-7}	10^{-6}	$2.1 \cdot 10^{-3}$	$7.4 \cdot 10^{-6}$	282
		10^{-8}	10^{-8}	$1.9 \cdot 10^{-7}$	$8.0 \cdot 10^{-10}$	243
	10^{-7}	10^{-7}	10^{-7}	$1.9 \cdot 10^{-4}$	$7.9 \cdot 10^{-6}$	24
		10^{-7}	$4 \cdot 10^{-7}$	$4.4 \cdot 10^{-3}$	$1.8 \cdot 10^{-4}$	25
		10^{-7}	10^{-6}	$2.1 \cdot 10^{-2}$	$7.4 \cdot 10^{-4}$	28
		10^{-8}	10^{-8}	$1.9 \cdot 10^{-6}$	$8.0 \cdot 10^{-8}$	24

Table 4.1: Coefficients used in some simulations. A and B state the maximum of the signals at ν and at 2ν respectively. the ratio A/B is useful to evaluate which signal is experimentally favorable.

The plot abtained with the coefficients of the first table's row ($a = 10^{-6}m$, $r = 10^{-7}m$, $\delta_x = 10^{-8}m$, $\Delta x = 10^{-7}m$) are reported in Figure 4.9 (signal at ν) and in Figure 4.10 (signal at 2ν). The shapes of the graphics related to the other parameters are similar.

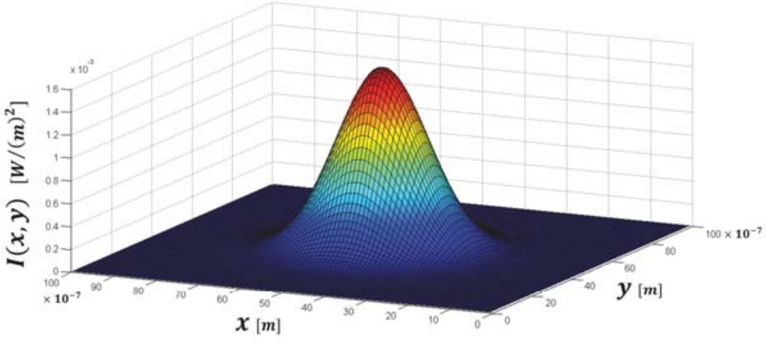

Figure 4.8: Normalized Gaussian intensity profile with parameter: $a = 10^{-6}m$, $P_i = 1\,W$.

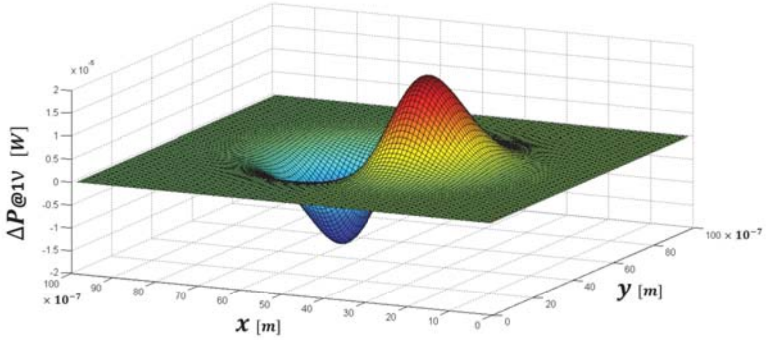

Figure 4.9: Signal at ν with parameters: $a = 10^{-6}m$, $P_i = 1\,W$, $r = 10^{-7}m$, $\delta_x = 10^{-8}m$, $\Delta x = 10^{-7}m$.

From Table 4.1we notice that an increase of the radius r cause a growth in the order of magnitude of booth of the signals A and B(as expected looking at Figure **??**and on physical basics). Even the signals ratio A/B grows: this means that for bigger disks' cross sections the signal A further increases with respect to signal B. From the

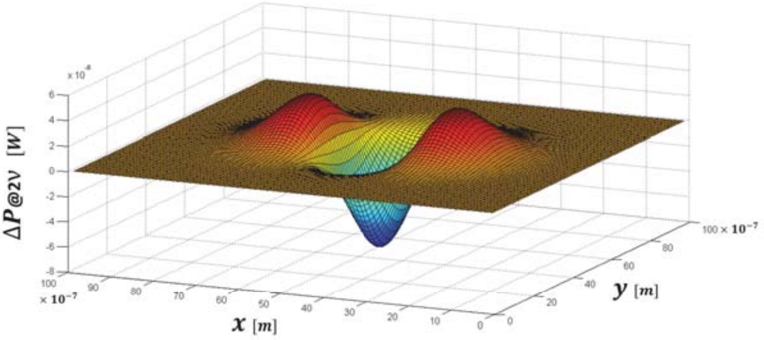

Figure 4.10: Signal at 2ν with parameters: $a = 10^{-6}m$, $P_i = 1\,W$, $r = 10^{-7}m$, $\delta_x = 10^{-8}m$, $\Delta x = 10^{-7}m$.

comparison between the A and B, we observe that it's always convenient to acquire the signal at ν, at least for sake of signal intensity. The last column of table 4.1 shows that the component oscillating at 2ν is one ore two order of magnitude lower than the signal at ν.

Under the hypothesis $\delta_x << a$, the maximum signals' changes over the entire cartography originated by an increase of the modulation's amplitude δ_x is dictated by Equations 4.12 and 4.13. Under this condition, one can explicit the dependence in δ_x:

$$A = A_0 \cdot \delta_x, \tag{4.14}$$

where $A_0 = \max \left\{ \left| \iint\limits_{disk} \left(\left. \frac{\partial I}{\partial x} \right|_{\substack{x=x'' \\ y=y''}} \right) dx''\, dy'' \right| \right\}$

and

$$B = B_0 \cdot \frac{\delta_x^2}{4}, \tag{4.15}$$

where $B_0 = \max \left\{ \left| \iint\limits_{disk} \left(\left. \frac{\partial^2 I}{\partial x^2} \right|_{\substack{x=x'' \\ y=y''}} \right) dx''\, dy'' \right| \right\}.$

Obviously signal A grows linearly with respect δ_x, while the signal B grows quadratically with respect δ_x.

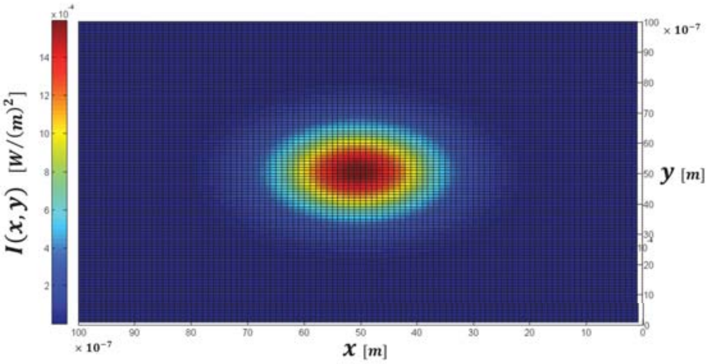

Figure 4.11: Bird's-eye view. Gaussian intensity profile with parameters: $a = 10^{-6}m$, $P_i = 1\,W$.

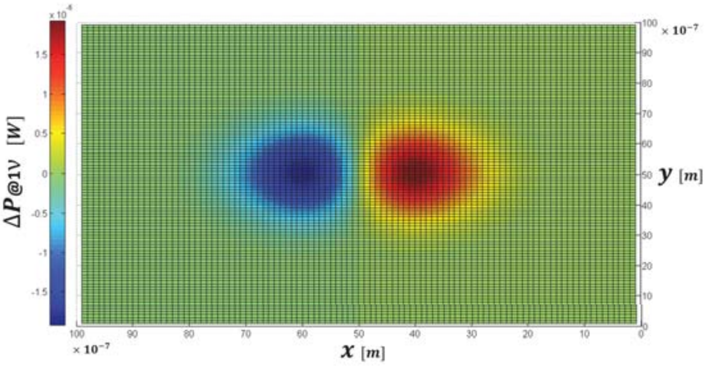

Figure 4.12: Bird's-eye view. Signal at ν with parameters: $a = 10^{-6}m$, $P_i = 1\,W$, $r = 10^{-7}m$, $\delta_x = 10^{-8}m$, $\Delta x = 10^{-7}m$.

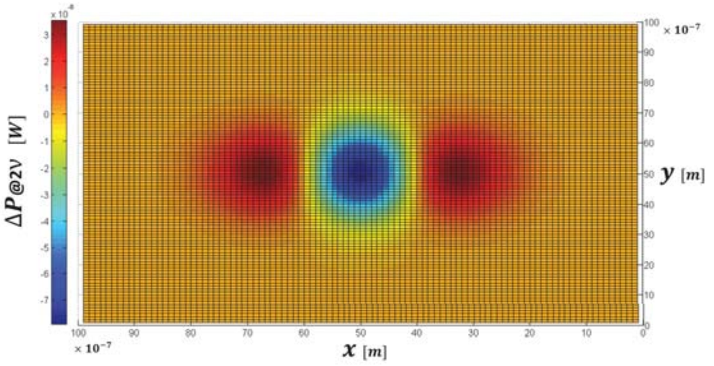

Figure 4.13: Bird's-eye view. Signal at 2ν with parameters: $a = 10^{-6}m$, $P_i = 1\,W$, $r = 10^{-7}m$, $\delta_x = 10^{-8}m$, $\Delta x = 10^{-7}m$.

It' useful, in view of the experimental implementation of the technique to valuate the dependences of the ratio $\frac{A}{B}$ from the main parameters. In particular from the acquisition parameters δx, Δx and from a and r variables. Following [38] the signal A and B can be cast in the following:

$$A = \frac{\delta_x}{\Delta x} \cdot A_{num}$$

and

$$B = \frac{\delta_x^2}{4\Delta x^2} \cdot B_{num},$$

see ref [38] for the definitions of A_{num} and B_{num}. And hence:

$$\frac{A}{B} = \frac{A_{num}}{B_{num}} \cdot \frac{4\,\Delta x}{\delta_x}, \tag{4.16}$$

where the ratio: A_{num}/B_{num} is a function of a and r.

4.3 Experimental realization

In order to implement the SMS technique we use a lock-in Amplifier(model 7265), a piezo, a piezoelectric controller, a SPM control unit[2], and the 1 MHz band output of the PDB430a photodetector.

---

[2] DAC, SPM acquisition software and pc.

The spatial modulation has been obtained using the internal oscillator of the Amplifier. The internal lock-in oscillator drives the piezo motor oscillation which ultimately drives the sample holder oscillation around it's equilibrium position. A scheme of the overall set-up is reported in figure 4.14. Let's describe the connections.

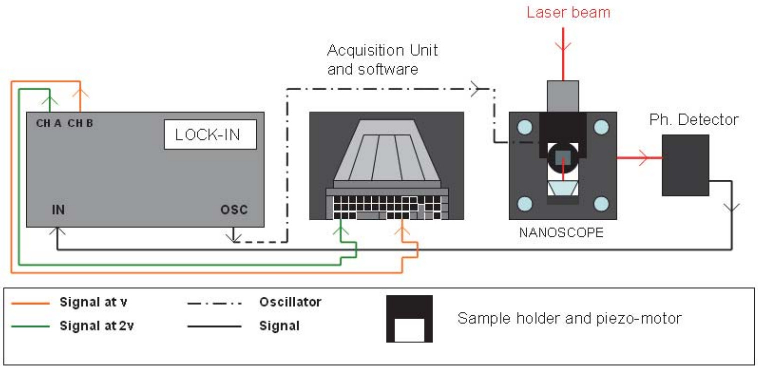

Figure 4.14: Bird's-eye view of the SMS' setup. The legend indicates the main connections. Signals at ν and at 2ν are labelled with the colors orange and green.

The channel which provides the oscillator signal is indicated as "OSC", and is labelled by a dotted line. The line "virtually" ends at the piezoelectric controller which is mounted under the sample holder. The signal recorded by the photodetector enters the input channel of the lock-in amplifier, called "IN" channel. The connection is represented by a continuous line. The lock-in performs the phase sensitive detection. The two signals leave the output channels of the lock-in, (Channel A and the Channel B), and enter the acquisition unit. The SPM control software processes them and composes the image.

4.3.1 Acquisition procedure

Once the devices and connections are set we start with the following procedures. With the help of the CCD camera we look for the right zone of the sample[3]. We should find the zone of containing the disk of desired size. We here report results obtained on sample B (Gold nanodisk). Before turning the modulation on we perform a raster scan, in order to visualize the disk's presence. Figure 4.15 shows position of 4 gold nanodisks when a $8x8\mu m$ area is scanned. Then perform the raster scan over a smaller area with the spatial modulation turned on (we turn on the lock-in amplifier). We chose an oscillator frequency compatible with the piezo motor and sample holder resonance frequency. The frequency has been fixed on the value of $20Hz$[4]. The amplitude of the modulation was varied from 10nm to 200nm. The oscillator provides a modulated voltage. The coefficient of proportionality between the set value of voltage on the lock-in and the real displacement of the piezoelectric actuator is $10\mu m/V$[5]. So 1 mV corresponds to a displacement of 10 nm.

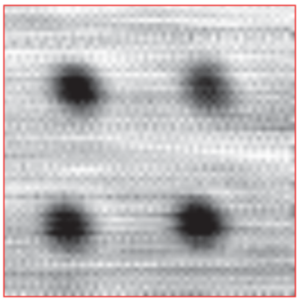

Figure 4.15: Imaging of four Gold nanodisks of 100nm diameter, obtained with maximum EBL. Tha scan area is $8x8\mu m$, 128 pixel of resolution and 50 ms of acquisition deley time.

---

[3] See the appendix, CCD camera.

[4] The piezoelectric actuator loaded with the sample holder has a resonance frequency at around 100 Hz

[5] We can consider a linear response up to 10V

We configured the lock-in amplifier in the dual harmonics mode[6]. In this way it's possible to detect at the same time the signal's components proportional to the first signal oscillating at ν and the second derivative signal oscillating at 2ν. We set the output time constant TC at the value of 200 ms[7]. The sensitivity was optimized. The dual harmonic mode of the lock-in allows us to simultaneously acquire the amplitude (R) of the signal components oscillating at ν and 2ν [8].

4.3.2 Experimental results

Let's start comparing the imaging in spatial modulation with respect the standard one. We define for convenience the imaging without spatial modulation as 0ν *imaging*. We talk about 1ν and 2ν *imaging*, when we record the AC component of the signal.
In figure 4.15 are visible four disk of $100nm$ diameter, that's what we see without spatial modulation (0ν imaging).

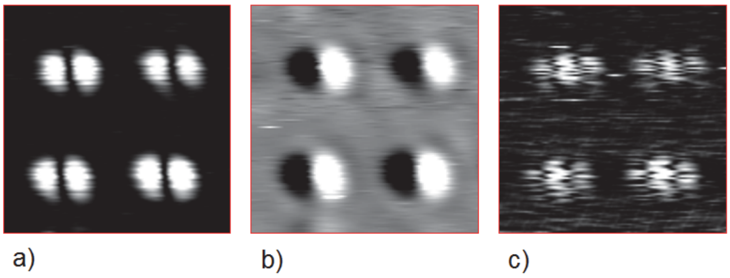

Figure 4.16: Imaging in spatial modulation of 4 Gold nanodisks of 100 nm diameter. Imaging performed with the laser beam @ 780. Figure a) is the module of the photovoltage at ν. Figure b) reports the component X of the photovoltage at 2ν, figure c) shows the module of the photovoltage at 2ν. The scan area is $8x8\mu m$, 128 pixel of resolution and 50 ms of acquisition delay time. Frequency of modulation is $20Hz$, $\Delta x = 62,5nm$, $\delta x = 100nm$.

The images in figure 4.16 report the 1ν and 2ν signals of the same area of fig. 4.15.

---

[6] See the appendix for specifications.

[7] The TC must be greater than the period of oscillation of the signal. In that case 20 Hz corresponds to 50 ms.

[8] Alternatively the component X and the phase or X,Y of a single harmonic.

Our principal aim is the detection of the nanodisks, the amplitude R is suitable for this purpose. For completeness we reported also the X component of the 1ν signal. We notice that, thanks to the presence of the two lobes, the 1ν imaging favors the location of the disk's center. Besides, comparing the contrast, the intensity of the 2ν signal appears, as expected, much lower than image a). To this end we pinpoint that the same sensitivity was used for both the signals at ν and 2ν.

Single Nanodisk

Once we focused on a single nanodisk, we acquired the signals at 1ν and 2ν varying the amplitude of modulation δx. The frequency of internal oscillator of the lock-in amplifier has been fixed on the value of $20Hz$. Scanning on a $4x4\mu m$ area with a resolution of $128x128$ pixels, one gets a value of $\Delta x = 23,4nm$. These parameters were fixed. The probe beam's waist was about $1\mu m$ as measured with the knife-edge.

We chose for the amplitudes of modulation the values: $1mV$, $10mV$ and $20mV$. The related displacements are $10nm$, $100nm$ and $200nm$. In order to compare the experiments with the theoretical evaluated signals A and B reported in table 4.1, we report the maximum voltage V used do compose the 1ν and 2ν imaging. We define $V_{1\nu}$ the maximum voltage relative to the 1ν imaging and $V_{2\nu}$ the maximum voltage relative to the 2ν imaging.

- **Amplitude** $\delta x = 10nm$

  The first measurement on a single nanodisk has been performed using $\delta x = 10$ nm. Even if we increased the sensitivity, neither the signal at 1ν or at 2ν was appreciable. The scan area was $3x3\mu$ m, 128 pixel of resolution. The acquisition delay time 50 ms, modulation frequency $\nu = 20Hz$, $\Delta x = 23.4nm$, $\delta x = 10nm$.

- **Amplitude** $\delta x = 100nm$

  Retaining the same parameters of the previous measurement except for δx, we obtained a considerable signal. In figure 4.17 we can observe the standard imaging (0ν) and the imaging of 1ν and 2ν. The maximum magnitude of the voltage acquired without spatial modulation, is $V_{0\nu} = 180mV$, while for 1ν we registered a maximum value of $V_{1\nu} = 3.3V$. The value of $V_{2\nu}$ is 0.014. This difference between $V_{1\nu}$ and $V_{2\nu}$ is appreciable in the higher chromatic contrast of the first image respect the second. Acquiring the 2ν signal individually we can increase the sensitivity of this specific channel. In that way it's possible to improve the chromatic contrast of 2ν imaging.

- **Amplitude** $\delta x = 200nm$

  The positive results obtained in the second case led us to further increase the modulation amplitude. The current value for $\delta x = 200$ nm, while the other conditions remain unchanged. The figure 4.18 shows clearly that the magnitude of the 1ν and 2ν are increased. In particular for the 1ν signal, $V_{1\nu} = 6.9V$ and for the $V_{2\nu} = 478mV$. White areas in the second and third images of figure 4.18 represents voltage's saturation. When the maximum voltage value exceeds the full scale the color of the affected area appears uniform and white.

Analysis of results

We compare the ratio of the amplitude A and B calculated by numerical simulation respect the maximum value of voltage $V_{1\nu}$ and $V_{2\nu}$. Table 4.1 report A and B in Watt, while the ratio is adimensional. Table 4.3.2 reports the parameters of the measurement and voltages of figure 4.17 and 4.18. Let's compare the measured ratio $V_{1\nu}/V_{2\nu}$ with the ratio A/B of the numerical simulations[9]:

a $[m]$	δ_x $[m]$	Δx $[m]$	$r[m]$	$V_{1\nu}[V]$	$V_{2\nu}[V]$	$\frac{A}{B}$
10^{-6}	10^{-7}	$23.4 \cdot 10^{-9}$	$10^{-}7$	3.3	0.14	23.5
10^{-6}	$2 \cdot 10^{-7}$	$23.4 \cdot 10^{-9}$	$10^{-}7$	6.9	0.47	14.6

Numerical simulations using a $\Delta x = 100nm$ and the same parameter a, $\delta x = 100$ and r of our measurements, estimated a ratio of 24. The ratio of maximum voltage $V_{1\nu}/V_{2\nu}$ that we obtained is 23.5. We can so consider that in that case experimental results are in agreement with the theoretical one. In the second case we adopt an oscillation amplitude

---

[9] See last column of the table 4.1

$\delta x = 200$ and measuring maximum voltages we get a ratio of 14.6. The Equation 4.16 suggests that A/B decreases with respect δx. This dependence is confirmed by the two values 23.5 and 14.6.

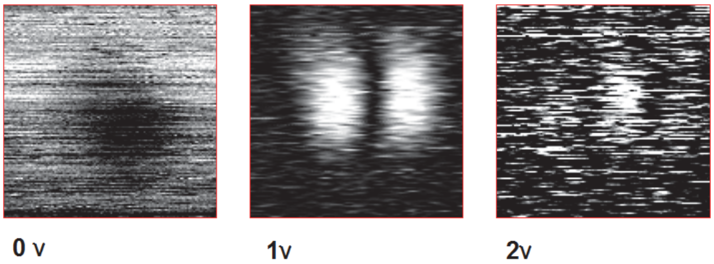

Figure 4.17: Imaging of a single nanodisk, $100nm$ diameter. The scan area is $3x3\mu m$, 128 pixel of resolution and 50 ms of acquisition delay time. Frequency of modulation is $20Hz$, $\Delta x = 23.4nm$, $\delta x = 100nm$. $TC = 200ms$ and sensitivity $= 5mV$.

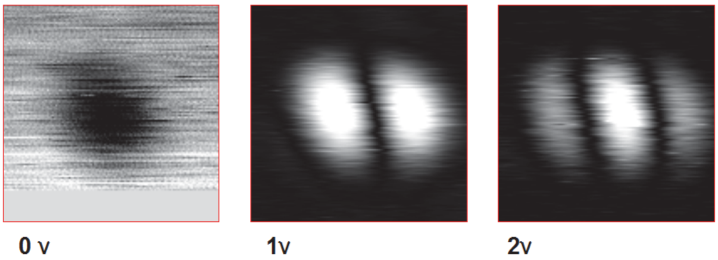

Figure 4.18: Imaging of a single nanodisk, $100nm$ diameter. The scan area is $3x3\mu m$, 128 pixel of resolution and 50 ms of acquisition delay time. Frequency of modulation is $20Hz$, $\Delta x = 23.4nm$, $\delta x = 200nm$. $TC = 200ms$ and sensitivity $= 5mV$. Figure 1ν and 2ν shows white areas which corresponds to a saturation of the signal.

Chapter 5

Pump & Probe measurements

First part of the chapter describes the disk's detection, that's the preliminary operation to perform the measurement. In the second section we report and discuss the experimental results.
Time resolved measurement have been conducted only on aluminum nanodisks.

5.1 Disks' detection

Exploiting the raster scan movement we can create a "cartography" of a micrometrical structure like the Knife-edge, or use it to characterize the beam. However scanning on a small object[1] as a nanodisck is quite different. The Knife-edge's width is about $50\mu m$, the disks' radius is about $400nm$, so they differs by two order of magnitude. The "ability"of an object to obscure the laser beam depends on its e.m. *cross section* σ. In turn $\sigma \propto r^2$[2]. Therefore we expect that the variation of voltage dispensed by the photodetector due to a scan on the Knife-edge is much more than the variation due to the nanodisk. For that reason the scan parameter must be setted differently, and the waist must be as small as possible. The detection and imaging has been always performed using the probe beam ($780nm$ wavelenght) .

Contrast and imaging

---

[1] Small with respect a structure as Knife-edge

[2] We consider r as the object's radius

Every area of Sample A which presents nanodisk is labelled by a marker[3] and a Knife-edge. Once we have placed the scan area in the vicinity of the the zone of the disks we start the search. We start looking for the disks of greater diameter, $460nm$. Figure 5.1 shows clearly the importance of the image contrast. When a disk crossed the beam the variation of the transmitted power is tiny. The voltage scale which constitutes the image must be restricted in order to underline the small variation of voltage. Reducing that range we change the grayscale, making possible to see small variations. We define ΔV as the difference $V_{max} - V_{min}$. The number of grey gradations is divided on that range ΔV. The imaging a) of figure 5.1 clearly shows two nanodisk and a Knife-edge. The parameters of scan are the same. The first way to reduced ΔV is lowering the beam's power by means of half-wave plate. The second way consist in a graphic processing. After the imaging has been executed we can vary the voltage scale, indeed the "contrast".

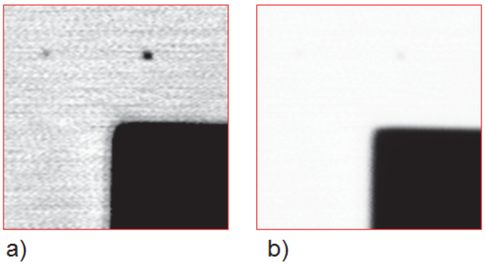

Figure 5.1: Comparison between two imaging on $460nm$ diameter nanodisks obtain through different voltage ranges. The scan area is $40x40\mu m$ and 128 pixel of resolution. The voltage scale ΔV of figure a) is $0,03V$, while for figure b) $\Delta V = 0,57V$.

Let's restrict the scan area on a single nanodisk. Figure 5.3 shows the beam imaging performed on a single aluminum nanodisk of 460 nm diameter. As we noticed previously when the beam's dimension exceeds the object we talk about *beam imaging*. For that reason, we stress that the imaging executed on a single nanodisk must be interpreted as the "shadow" of the beam and not as a photography of the disk.

---

[3] See the section "Samples".

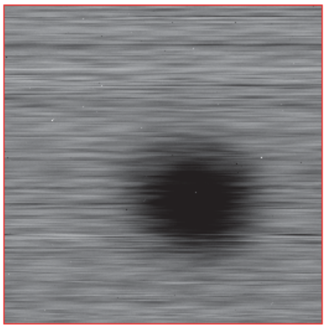

Figure 5.2: Probe beam's imaging trough a single nanodisk. The scan area is $5x5\mu m$, the resolution $256x256$ pixel and $\Delta V = 0.048V$

In order to perform pump & probe measurements three condition must be met. First centering of the probe beam on the single disk must be accomplished. Second the probe beam waist must be less than the distance between adjacent disks. This condition is met engineering the sample so that the nanodisk's array periodicity exceeds the probe beam waist. The centering must be execute using the SPM control's panel, which enable to move the scan area with a precision of few nanometers. The preliminary operations described in the appendix (See *alignment of the beams*) allows meeting the latter. Third the probe beam must be "contained" in the pump beam.

5.2 Time resolved measurement on a single nanodisk

Once the beams are correctly positioned, we begin to measure with the Asops system. A single laser pump's pulse excites the disk, delivering the energy density δU. The energy absorbed first heats the electrons, the electrons then thermalize with the disk's phonons. The lattice's temperature increases from T to $T + \Delta T$ inducing a thermal expansion of the nanodisks. The effect of the electrons heating is a variation of the dielectric constant leading to an increase of the extinction cross section σ_{ext} of the disk. Such process result in a temperature dependent variation of the transmissivity with respect the equilibrium value. As the cooling process takes place and σ_{ext} return to the unperturbated value the thermalization of the disk with the substrate ends, the variation of relative transmission, $\frac{\Delta Tr}{Tr}$, goes to zero.

We can measure two photovoltages on two different channels. The"RF Output" channel of the photodetector provides a voltage proportional to the variation ΔTr. Such variation is acquired when the pump beam excite the sample. The absolute value of Transmissivity Tr is proportional instead to the voltage provided by the channel "Monitor+". In order to get the relative variation $\frac{\Delta Tr}{Tr}$ we needs both channels. The two photodetectors' channel operates a different conversion V/W, the difference among two conversion is 1.7. In the present work we are not interested in the exact value of the ratio $\frac{\Delta Tr}{Tr}$, but in the relaxation times. For that reason, an error due to a factor of 1.7, can be neglected. The first step of the measurement consists in measuring ΔTr, averaged on n scans. In the second step we measure the "ground". That signal consists in the photovoltage due to the probe beam (on the RF output channel) in absence of the the pump beam. The differences between the first measure and the ground, provides the real measurement of the variation ΔTr.

Analysis and curve fitting

Let's analyze the result of a typical measure. The plot in figure 5.3 shows the relative variation of $\Delta Tr/Tr$, due to a $460nm$ Al disk. The signal ΔTr has been divided by the value $Tr = 1.07V$. The ground signal, not present in the plot, was subtracted. The power of the pump beam before entering the Nanoscope was $36,4mW$. Considering the total losses[4], the incident power on the sample plane was $29mW$. The pump waist was $w_{=}1.4\mu m$, so the energy per pulse was $47J/m^2$. The probe power to be $0.11mW$. The probe waist was $w_0 = 0.9\mu m$, so we estimate an energy per pulse $0.43J/m^{25}$.

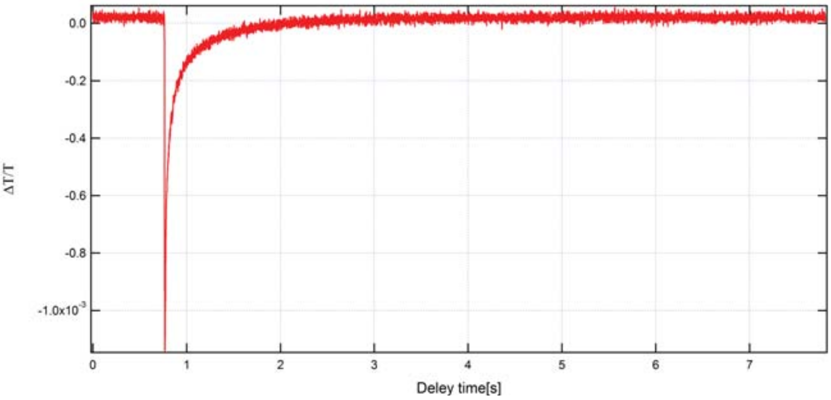

Figure 5.3: Relative variation of transmission with respect the time delay. Aluminum disk of 460 nm diameter. Probe beam's $w_0 = 1\mu m$, the FWHM is $\sim 1.2\mu m$. The detuning $\delta\nu = 10007Hz$, and led to a resolution of $1ps$.

We set a detuning frequency $\Delta\nu = 10KHz$ in order to decrease the amplitude of the noise. Setting an high detuning frequency the temporal resolution decrease, but for equal time of sampling, we can integrate the signal many more times.

To extrapolate the time scales of the the thermal dynamics involved, we fit the curves

---

[4] We consider a loss due to each gold mirror and to the HR mirror of 2% and the loss due to the focusing objective of 10%.1

[5] We considered the waist as the beam's radius

using a linear combination of three exponential:

$$f(t) = A \cdot exp(t/\tau_1) + B \cdot exp(t/\tau_2) + C \cdot exp(t/\tau_3)$$

We performed the fit on the normalized curve[6] of plot 5.3. Figure 5.4 reports the normalized $\Delta Tr/Tr$ and the fit function. The decay times with the 95% confidence bound are: $\tau_1 = 8.8ps(8.42ps, 9.38)$, $\tau_2 = 78ps(75.4, 81)$, $\tau_3 = 0.59ns(0.58, 0.6)$.

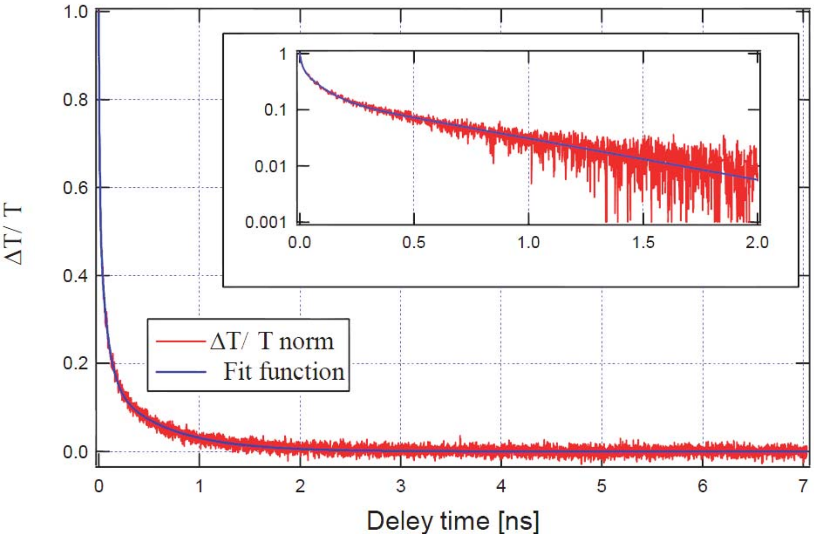

Figure 5.4: Relative variation of transmission (normalized) with respect the time delay (red curve). The fit function blu curve. Inset: The same curves in semi-log scale up to a delay time of 2ns. Aluminum disk of 460 nm diameter. Probe beam's $w_0 = 1\mu m$, the FWHM is $\sim 1.2\mu m$. The detuning $\delta\nu = 10007Hz$, hence a resolution of $1ps$.

The value $\tau_3 = 590ps$ is comparable with the estimate evaluated in second chapter where the calculated value for the theoretical heat transfer from the nanodisk to the substrate was $700ps$. The inset of figure 5.4 shows the same trace, but in logarithmic scale. The first dynamic, $\tau_1 \sim 8,8ps$, although rather long, can be compatible with the e-ph relaxation time within the Al nanodisk. The second dynamic, $\tau_2 = 78ps$, is

---

[6] The curve has been normalized with respect the maximum value.

unexpected and we don't have an explanation for it at present.

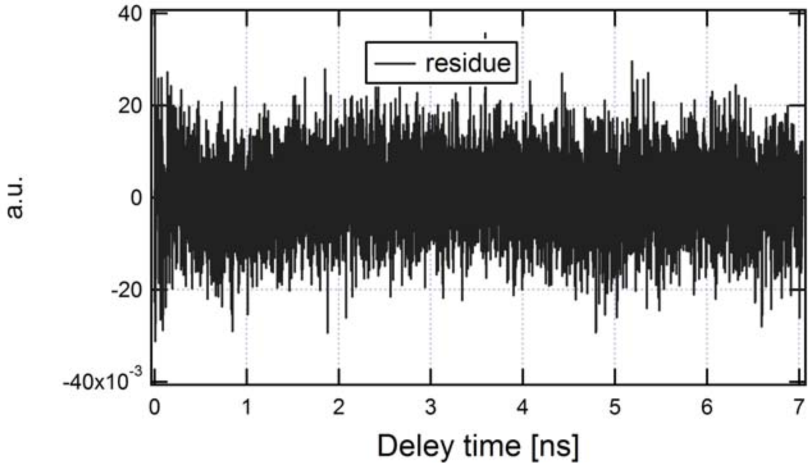

Figure 5.5: Residue of the fit reported in figure 5.4

Many performed measurements have not be studied yet. Since we managed to perform pump and probe measurements on a single metallic nanodisk with the Asops system, a new field on investigation has been opened.

Chapter 6

Conclusions and perspectives

The scope of this thesis work has the implementation of a spatially modulated nanoscope based on asynchronous optical sampling for the realization of time-resolved optical measurements on a single metallic nanostructure with dimensions inferior to the wavelength. The field of investigation is the thermodynamics of mesoscale systems. The time of thermal transfer from metallic nano-object to the substrate depends on the linear dimensions of the former. In a mesoscopic sample such dynamics usually takes place in a time interval in the order of 10 ns. The traditional time-resolved spectroscopy set-up based on line delay is hardly practicable on such time scales, hence in the present work we opted for an Asops system. Time-resolved optical microscopy to be performed on mesoscale systems made it necessary to implement an imaging apparatus for spatial modulation. The latter was implemented in a Nanoscope system. After this implementation we were able to detect and place the pump and probe beams on a single metallic nanostructure with dimensions way inferior both to the pump and the probe wavelength.

This result, along with the implementation of the diagnostics of the laser beams focused to the diffraction limit, allowed measuring the thermal dynamics from a metal nanodisk to the substrate over four time decades ranging from 1 ps up to 10 ns. The up-grades for seen for the near future consist in (a) implementing an higher modulation frequency. This will improve the signal-to-noise ratio and speed-up the spatial modulation imaging process (b) implement a beam guiding scheme al based on fiber optics. These improvements will allow investigating the thermomechanics of single nano-objects with unprecedented ease and high measuring through output.

Appendix A

Electronics and devices

A.1 High-speed Photodetector

Let's see the characteristics of the electronic devices that we used for data acquisition. We detect leaser beams trought two different photodetectors. We used both a InGas photodetector and a Balanced Amplified Photodetector (two channels), that hereinafter we will calll *differential Photodetector*. The Asops system requires the differential detector. We have to acquire the *signal difference* between the intensity of the tramitted beam and of the *reference* beam. Only the probe is detected. The features of this devices must match our measurement needs. In particular, we need an elevated time resolution and low noise.

Differential photodetector: PDB430A, PDB430C [26].
The PDB4xx series Balanced Amplified Photodetectors consists of two wellmatched photodiodes and an ultra-low noise, high-speed transimpedance amplifier that generates an output voltage (RF OUTPUT) proportional to the difference between the photocurrents of the two photodiodes, i.e. the two optical input signals. Additionally, the unit has two monitor outputs (MONITOR+ and MONITOR-) to observe the optical input power levels on each photodiode separately.[1].

---

[1] If we measure the voltage from the channel MONITOR+, that is different from the voltage we can measure on RF-OUTPUT channel with input stopped

Let's focus on the electronics, a functional block diagram is schematized in Fig. A.1. The PDB4xx series is powered by the external power supply (±12 V, 200mA).The main features of photodetectors are reported in tables A.1 and A.2. Table A.1 lists common thecnical data, Table A.2 lists individual characteristics. The beams' intensity must be checked to avoid damaging the photodiodes.

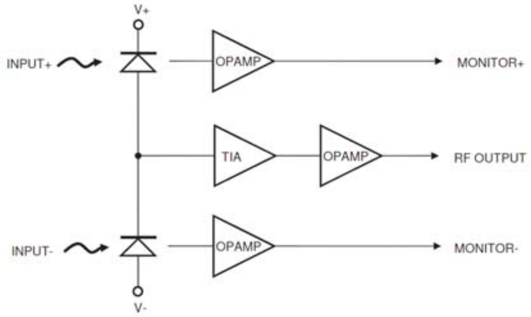

Figure A.1: 350 MHz Balanced Amplified Photodetector PDB4xx.

Common features	
Max. Input Power	20 mW (photodiode damage threshold)
RF-Output Impedance	50ω
RF OUTPUT voltage swing, max.	± 3.6 V (high impedance load) *)
Monitor Output Impedance	220 Ω
Monitor Output Bandwidth	DC 1 MHz
Conversion Gain Monitor Outputs	10 V/mW @ peak responsivity
Monitor Output voltage noise	180 $\mu VRMS$
DC-offset MONITOR Outputs	¡ +/-2 mV
Size	85x80x30 mm^3
Power Supply	+/-12 V, 200 mA

Table A.1: Common features of the PDB4xx series.

Individual features		
	PDB430A	**PDB430C**
Detector Material/Type	Si / PIN	InGaAs / PIN
Wavelength Range	$320nm - 1000nm$	$800nm - 1700nm$
Typical Max. Responsivity	$0.5A/W$	$1A/W$
Detector Diameter	$0.4mm$	$0.15mm$
RF-Output Bandwidth (3dB)	$DC - 350MHz$	$DC - 350MHz$
Transimpedance Gain	10 x 103 V/A	10 x 103 V/A
Conversion Gain RF-Output	$5x10^3V/W$	$10x10^3V/W$
CW Saturation Power	$720\mu W@820nm$	$360\mu W@1550nm$
Overall output voltage noise	$1.5mVRMS$	$1mVRMS$

Table A.2: Individual features of the PDB4xx series .

A.2 Lock-in Amplifier

A.2.1 Operative principles

The SMS technique requires a lock-in. As previously observed in chapter four, relative variation of the transmition $\Delta T_{ext}/T_i = (P_t - P_i)/P_i$, as obtained in the SMS, includes oscillating components at ν and at 2ν. The voltage delivered from the photodetector is extremely small ($\sim \mu V$) and hidden in noise. If we want to detect that signal oscillating at the frequency ν and at 2ν, we need a *phase-sensitive detection* (PSD)[2] A lock-in amplifier is an electronic devices which can detect and measure low AC signal filtering noise. Thanks to this pivoltal instrument we performed measures of spatial modulation on a single nanodisk. Let's report and analyze basic the principles of *phase sensitive detection*. The measurement requires setting a reference frequency[3]. In our case we exploit the internal oscillator of the lock-in amplifier.

Let's define the **measured signal**, and the **reference signal** as:

---

[2] .

[3] This frequency ν corresponds to the modulation frequency given by the piezo motor

$$\begin{aligned} V_s(\omega_s) &= V_s \sin(\omega_s t + \theta_s) \\ V_r(\omega_r) &= V_r \sin(\omega_r t + \theta_r) \end{aligned} \tag{A.1}$$

The first block of the lock-in amplifiers detected signal $V_s(\omega_s)$ and multiplies it with the reference signal. The output of the phase sensitive detector is :

$$\begin{aligned} V_{psd} =& V_s V_r \sin(\omega_s t + \theta_s) \sin(\omega_r t + \theta_r) \\ =& \frac{1}{2} V_s \cos[(\omega_s - \omega_r)t + \theta_s - \theta_r] - \frac{1}{2} V_s \cos[(\omega_s + \omega_r)t + \theta_s + \theta_r] \end{aligned} \tag{A.2}$$

The purpose of the PSD and LowPass filter is to extract only frequencies near to ω_r, set by the reference, and filter the noise. A lowpass filter blocks the frequency components which differ from the reference frequency ω_r in the following way. The output A.2 consist in two AC signals, one has the frequency difference $\omega_s - \omega_r$ and the other the sum $\omega_s + \omega_r$. The LP filter has a narrow frequency band centered at $\omega = 0$, indeed only the AC components $\omega \sim \omega_r$ passes. The signal which survives from the filter consists of a DC signal :

$$V_{psd} = \frac{1}{2} V_s V_r \cos(\theta_s - \theta_r) \tag{A.3}$$

The phase's dependence is removed introducing another reference $\pi/2$ out of phase with the previous one. The two DC signals are defined as X and Y, the first is called "component in phase" and the second is called " squaring". The amplitude of the signal that we measure with the lock-in devices is:

$$R = \sqrt{(X^2 + Y^2)} = V_s \tag{A.4}$$

This provides the amplitude of the measured signal and it shows no dependece from the phase.

A.2.2 Specification and Filter's characterization

Taking a reference signal of $1V$, and using a oscilloscope, we characterize the line filters in order to observe the frequency attenuations. The **OSC OUT** was directly inserted in the input **channel A**. In the first column of the next table are reported the frequency values of the signal, in the second we list the voltage values for every frequency. Values list in the table are reported in graph A.2.

Line Filter characterization ($V_{in} = 1V$)			
Frequency	V_{out}	**Frequency**	V_{out}
$10Hz$	$990mV$	$20Hz$	$950mV$
$30Hz$	$845mV$	$40Hz$	$557mV$
$50Hz$	$11mV$	$60Hz$	$440mV$
$70Hz$	$556mV$	$80Hz$	$483mV$
$90Hz$	$282mV$	$100Hz$	$10mV$
$150Hz$	$763mV$	$200Hz$	$903mV$

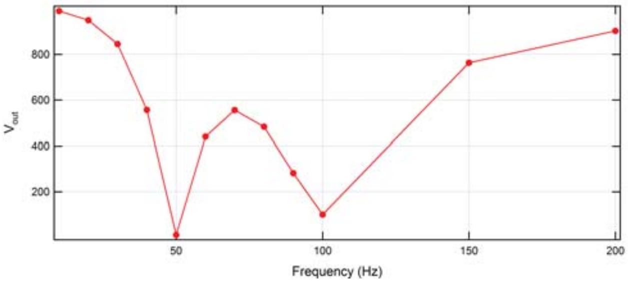

Figure A.2: Line filter characterization.

The amplifier is equipped with **dual reference** and **dual harmonics** mode. In the first mode (dual reference) the instrument can take simultaneous measurements of two signals at different reference frequencies. The dual harmonic mode allows to use two different harmonics of the internal oscillator as reference signals. We adopted that mode to measure at the same time the $1f$ and $2f$ signals.

A.3 CCD color camera

In order to facilitate the movements of the laser beam on specific areas of the sample, we used a *CCD USB Color camera*[4]. The deviced is placed on the top of the Nanoscope, as shown in figure 3.4. Exploiting the focalizin nanoscope's objective, it's possible to observe the sample with a fixed magnification in real time. For semplicity, we consider the *50x Nikon Objective* as a lens which reporoduces an object on the CCD's sensor. The mechanism of image creation which considers the objective as a compound lens, has not been dealt with.

We derived the magnification of the system camera + objective as follow. Figure A.3 reports the shape and dimension of the camera's sensor.

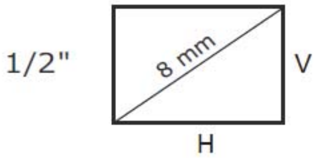

Figure A.3: Shape and size of the CCD's sensor.

The total pixels are $1360x1024$, each pixel size is $4.65x4.65\mu m$. We compared the dimension of a real object with respect the dimension of the image formed on the sensor. The lenght of the H side is 6.324 mm, while the object's lenght which image cover the entire extent H on the CCD, is 0.18 mm. We reach a magnification of:

$$M = \frac{3.324}{0.18} = 35$$

It's necessary to illuminate the area that we want to oserve, by means of an external light source. Materials with a high reflectivity can be observed with the CCD just using the laser source. Gold has 98% reflectivity in the infrared region, all this makes the sample B's marker easily identifiable. Figure A.4 reports the effect on the image obtained with three different kinds of illumination.

---

[4] The model that we used is $DFK41AU02$

a) Sample illuminated by laser beam (780 nm wavelenght).

b) Illumination in reflection exploiting white leds.

c) Illumination in transmission using white light.

Figure A.4: Images acquired with the camera, using different kinds of lighting.

Appendix B

Sample's Fabbrication Process

This Appendix describe describes the aluminium nanodisk's fabrication process. The sample was fabricated by M.Travagliati at the nest Lab. in Pisa.

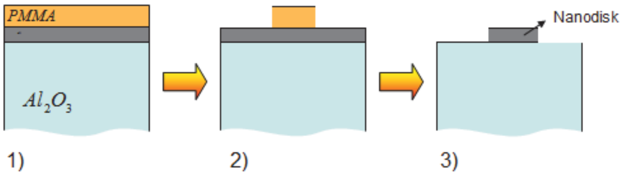

Figure B.1: Diagram of the fundamental steps involved in the sample nanofabrication process. The resist is PMMA , the aluminum layer 2 and the substrate sapphire.

The procedures in schematized in figure B.1.

1. After the cleaning, an proper aluminium substrate of proper dimension is evaporated on the substrate (Al_2O_3). The surface is coated with a temporary layer of negative e-beam resist.
2. The electron beam in scanned across the resist surface in a pattern which is complementary to the Al disk array which will be finally obtained. In order to obtain only the exposed area of the resist, we put the sample in the developer solution for necessary amount time (development). We obtain the configuration illustrated

in point 2.

3. The Al is etched with a process of dry-etching called *RIE*[1] with a clorine plasma. The process removes aluminum where the resist is not present on the surface. The sample is put in a resist solvent, acetone. The resist left on the surface is washed out, leaving only the Al

In order to make sure that there is nothing left apart nanodisk, a cleaning with a plasma Oxygen has been made.

---

[1] Reactive Ion Etching

Appendix C

Nanoscope operating procedures

This section shows how to configure the set-up in order to achieve the sample imaging and *pump* and *probe* measurements.

- **Alignment of the beams** The pump and the probe beam are collimated and spatially overlapped before the entering the nanoscope.
- **Nanoscope's Optimization**

  Thw next step is the positioning of the objectives. We exploit the probe beam only for this operation.

  We start from the top of the Nanoscope. The HR mirror must be set at 45 respect incidet beam The basis of the tripode mus be levelled. Our aim is drive the laser beam through the two objectives. We use two pinholes to center the beam. Moreover it's important that the distance between the two objectives and the sample is the same.
- **Search of the height's minimum *waist*** We want to determine the minumum waist w_0[1] of the pump and probe's beam, exploiting the Knife-edge. The **Manual method** is the follow.

  Once the beam is centered on the knife-edge which lay on the plane of the sample, we put an infrared sensor at the exit of the nanoscope. The beam profile looks like

---

[1] We have defined the coordinate of minumum waist w_0, z_0

a circular spot, where a portion is darked by a rectangular shadow. Translating the sample along the x axis, the rectangle can cut the beam's profile in two different ways. The edge can enter along the positive x direction or along the opposite direction. We can demostrate that the direction of entry of the edge depends from the height of thecut z versus the location z_0 of the minimum waist. Figure C.2 shows the situation. The inversion height of the direction of entry defines the exact coordinate z_0. The closer we get to z_0, more the shadow of the knife edge obscure the beam profile. Keeping this in mind we approch as much as possible height at which the minimum waist is positioned. We can cut the beam in two ways: through the manual sledge, (micrometer screw) or using using the motorized movement of the raster scan.

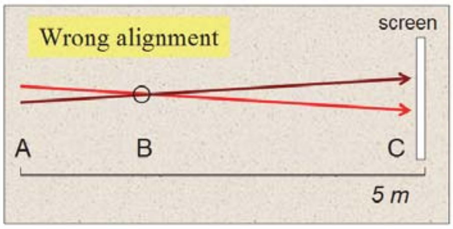

(a) Alignment wrong

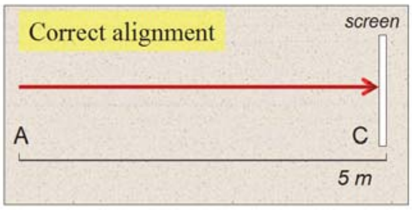

(b) Alignment correct

Figure C.1: In figure (a) the beams start from the point A, coincide in a point B and arrive on the screen (point C). The beams are not parallel. In figure (b) beams are properly aligned.

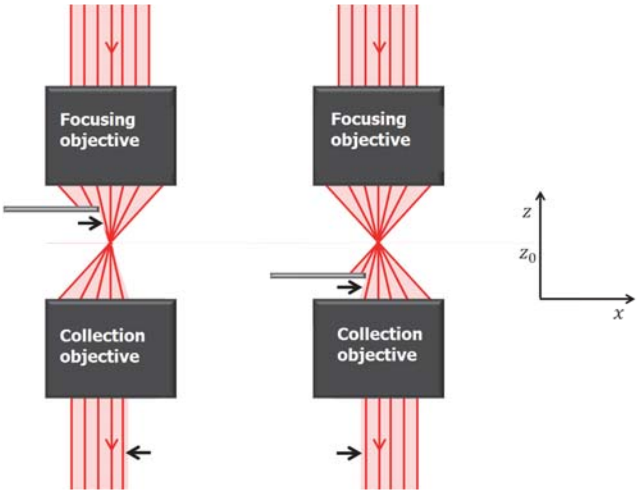

Figure C.2: Beam's cut by the knife-edge. Difference between the two height of entry, above and below z_0 (Waist minimum' posotion).

Appendix D

Acronyms

ASOPS	*Asynchronous Optical Sampling*
δU_V	*energy density absorbed by the pump pulse*
δQ_V	*energy density released to the substrate*
$g(\mathbf{r}, t)$	*source of power density*
$\mathbf{q}$	*thermal current density*
ρ	*mass density*
c_m	*specific heat for unity of mass*
κ	*thermal conductivity*
Λ_{Al}	*penetration dept of our laser pump in Aluminum*
T_{sub}	*substrate temperature*
ρ_{th}	*thermal boundary resistance*
B	*Biot number*

J_p	*heat flux between nanoparticle and substrate*
N.A.	*numeric aperture*
f	*focal lenght*
z_i	*initial height of the multi raster scan*
z_f	*final height of the multi raster scan*
N	*number of scanned plans*
λ	*wave lenght*
$w(z)$	*waist*
w_0	*minimum waist*
z_0	*height of minimum waist*
z_R	*Rayleigh range*
M^2	*parameter which indicates the difference between the real and ideal beam*
θ	*angle of focusing*
P	*power*
$\frac{dE}{dS}$	*energy per pulse per unit area*
τ	*rate of decay*
K	*constant tau dependent*
U.A.	*arbitrary unit*

U.A.L.	*arbitrary lenght unit*

Acknowledgments

I would like to thank my advisor Francesco Banfi who helped and guided me during this thesis work. I wish also thank all the people working in the laboratory, in particular Fabio Medeghini. A special thanks goes to Simona, and to my family, in particular to my sister Alessandra.

Bibliography

[1] L.R. Hirsch, R.J. Stafford, J.A. Bankson, S.R. Sershen, B. Rivera, R.E. Price, J.D. Hazle, N.J. Halas, and J.L. West, *Proc. Natl. Acad. Sci. U. S. A* **100**, 13549 (2003).

[2] P.K. Jain, I.H. El-Sayed, and M.A. El-Sayed, *Nanotoday* **2**, 18 (2007).

[3] L. Paasonena, T. Laaksonenb, C. Johansb, M. Yliperttulac, K. Kontturib, and A. Urttic, *J. of Controlled Release* **122**, 86 (2007).

[4] M. Rini, A. Cavalleri, R. W. Schoenlein, R. Lopez, L. C. Feldman, R. F. Haglund Jr., L A. Boatner, and T. E. Haynes, *Opt. Lett.* **122**, 558 (2005).

[5] A. Canteri, "Studio di fattibilità di una microscopia ottica risolta in tempo basata su tecnica ASOPS", Tesi di Laurea in Fisica, Università Cattolica del Sacro Cuore, A.A. 2010-2011.

[6] C. Giannetti, F. Banfi, D. Nardi, F. Ferrini and F. Parmigiani, *IEEE Photonics Journal* **1**, 20 (2009).

[7] F. Banfi, F. Pressacco, B. Revaz, C. Giannetti, D. Nardi, G. Ferrini and F. Parmigiani, *Phys. Rev. B* **81** 155426 (2010).

[8] www.nist.gov/data/nsrds/NSRDS-NBS-8.pdf.

[9] M.J. Weber *Handbook of optical materials* CRC Press, 2003.

[10] F. Pressaco *Studio di fattibilità per una tecnica completamente ottica per misure nanocalorimetriche*, Università di Trieste, Master Thesis (2008); http://www.dmf.unicatt.it/elphos/.

[11] F. Medeghini *Microscopia ottica risolta in tempo su singolo nanodisco*, Universitá cattolica di Brescia, Tesi Triennale (2012).

[12] Stoner1993: R. J. Stoner and H. J. Maris, Phys. Rev B 48, 16373 (1993).

[13] F. Banfi, V. Juvé, D. Nardi, S. Dal Conte, C. Giannetti, G. Ferrini, N. Del Fatti, and F. Vallée, *Appl. Phys. Lett.* **100**, 011902 (2012).

[14] Siemens, M. E.; Li, Q.; Yang, R.; Nelson, K. A.; Anderson, E. H.; Murnane, M. M.; Kapteyn, H. C. Nat. Mater. 2010, 9, 26.

[15] C. Giannetti, B. Revaz, F. Banfi, M. Montagnese, G. Ferrini, F. Cilento, S. Maccalli, P. Vavassori, G. Oliviero, E. Bontempi, L. E. Depero, V. Metlushko, and F. Parmigiani,*Phys. Rev. B* **76**, 125413 (2007).

[16] Menlo System, *ASOPS white paper*, April 15 2009.

[17] A. Comin, C. Giannetti, G. Samoggia, P. Vavassori, D. Grando, P. Colombi, E. Bontempi, L. E. Depero, V. Metlushko, B. Ilic, and F. Parmigiani *Phys. Rev. Lett.* **97**, 217201 (2006).

[18] D. Nardi, M. Travagliati, M. E. Siemens, Q. Li, M. M. Murnane, H. C. Kapteyn, G. Ferrini, F. Parmigiani, and F. Banfi, *Nano Lett.* **11**, 4126 (2011).

[19] M. Travagliati, *Fabrication and time-resolved optical investigation of hypersonic phononic crystals*, Università Cattolica del Sacro Cuore, Master Thesis (2007); http://www.dmf.unicatt.it/elphos/.

[20] A.Lombardi, *Proprietá ottiche di singole nanoparticelle metalliche*, Università Cattolica del Sacro Cuore, Master Thesis (2010)

[21] M. Travagliati, D. Nardi, F. Banfi, V. Piazza, and P. Pingue, *Thermomechanical decoupling in hypersonic phononic crystals*, MNE 2010 - 36th International conference on Micro & Nano Engineering: September 19-22, 2010, Genova (Italy).

[22] V. Juvé, M. Scardamaglia, P. Maioli, A. Crut, S. Merabia, L. Joly, N. Del Fatti, and F. Vallée *Phys. Rev. B* **80**, 195406 (2009).

[23] Xiaohua H.,Prashant K Jain, Ivan H El-Sayed and Mostafa A El-Sayed, *Gold nanoparticles : interesting optical properties and recent applications in cancer diagnostic and therapy*, *review*, *Nanomedicine*, 2007.

[24] G. V. Hartland, *Chem. Rev.* **111**, 3858 (2011).

[25] O. L. Muskens, N. Del Fatti, F. Vallée, *Nano. Lett.* 6, 552 (2006).

[26] Thorlabs Instrumentation Operation Manual, ”Balanced Amplified Photodetectors PDB400 Series”; http://www.thorlabs.com

[27] Thorlabs Instrumentation Operation Manual; http://www.thorlabs.com

[28] Catalog Datasheet Piezo Nano Positioning; http://www.physikinstrumente.com/en/pdf/-P611_XZ_Datasheet.pdf.

[29] http://www.edmundoptics.com/imaging/imaging-lenses/fixed-magnification-lenses/nikon-cfi-60-infinity-corrected-brightfield-objectives/2690.

[30] www.quartz-silica.net/sapphire.htm.

[31] A. Yariv, *Quantum Electronics*, 3ed., Jhon Wiley and Sons, 1989.

[32] Gaussian Beams and the Knife-Edge Measurement; http://massey.dur.ac.uk/resources/grad_skills/KnifeEdge.pdf.

[33] J. B. Pendry, *Negative Refraction Makes a Perfect Lens*, (2000); http://www.pi5.uni-stuttgart.de/de/teaching/lectures/show_file.php/lectures/74/prl2000-pendry.pdf.

[34] Melles Griot Documentation, *Introduction to Gaussian Beam Optics*, (2009); http://www.capem.buffalo.edu/lab-manuals/MG-GaussianBeams.pdf.

[35] E. D. Swartz and R. O. Pohl, *Rev. Mod. Phys.* **61**, 605 (1989).

[36] O. Muskens, D. Christofilos, N. Del Fatti & F. Vallée, *J. Opt. A: Pure Appl. Opt.* **8**, S264 (2006).

[37] Equipe FemtoNanoOptics, N. Del Fatti & F. Vallée, Institut Lumière Matière, CNRS – Université Lyon 1

[38] Fabio Medeghini, *Spatial Modulation Spectroscopy*, integrative work for F credits.